

1 Seismic wave-based constraints on geodynamical processes: an 2 application to partial melting beneath the Réunion island

3 **T. Franken¹, J.J. Armitage^{1*}, N. Fuji¹, A. Fournier¹**

4 ¹Université de Paris, Institut de Physique du Globe de Paris, CNRS, F-75005 Paris, France

5 *Now at: IFP Énergies Nouvelles, 1 & 4 avenue de Bois Préau, 92852, Rueil-Malmaison Cedex, France

6 **Key Points:**

- 7 • We combine geodynamic modeling with seismic wave propagation to constrain the
state of the dynamics underneath the Réunion island.
- 8 • We analyze the sensitivity of seismic observables to geodynamical parameters.
- 9 • Our results favor high melt extraction rates underneath the Réunion island.

11 **Abstract**

12 The inversion of seismic observations leads to maps of the interior of the Earth that can
 13 be interpreted. Regions of low seismic velocity have historically been interpreted to be
 14 due to factors related to high temperature and high melt retention. Subsequently, geody-
 15 namic models can be used to test such interpretations. However, the inversions are non-
 16 unique, and arguably it would be best to test geodynamic scenarios against observations
 17 rather than interpretations. Here we make a first attempt at this. At depths greater than
 18 80 km below Réunion a low shear-wave velocity zone is imaged. Rather than interpret
 19 this inverted model, we test a forward model of melt generation and retention against seis-
 20 mic observations. Geodynamic model solutions are converted with a mineral parameter
 21 database to P- and S-wave velocity profiles from various initial temperatures T , upwelling
 22 velocities \bar{v} and permeabilities k_0 . By embedding these velocity profiles, synthetic seis-
 23 mograms are generated. For a range of k_0 , T and \bar{v} , we generate synthetic traces for 21
 24 teleseismic events registered at a receiver on Réunion island. We measure the traveltimes
 25 difference between observed and synthetic waveforms, and the inter-phase differential trav-
 26 eltimes for 210 scenarios for several phase arrivals of three components, filtered between
 27 0.01 and 0.2 Hz. The results indicate that upper mantle temperatures beneath Réunion lie
 28 within 1400-1450 °C, with permeability coefficients of 10^{-5} - 10^{-6} m². These conditions
 29 are associated with porosities of <0.28% and high melt extraction rates of 8.37-18.35
 30 m yr⁻¹. This study demonstrates the potential for fully comparing geodynamic scenarios
 31 with seismic observations.

32 **1 Introduction**

33 The geodynamical evolution of planetary interiors at any scale has been constrained
 34 by observations made at and/or above the surface of the Earth and planets. Seismological
 35 observations, for example, can give some information in the form of a “snapshot” of the

36 structure of Earth's interior. However, it is seldom the seismological parameters that the
 37 geoscience community really wants to know, rather we use them to attempt to understand
 38 thermo-chemical conditions of the planetary interior and their evolution. This is why most
 39 of the studies on the Earth's interior have been based on inversions of such observations.
 40 Here we briefly review the classical inversion procedures. We then present our method-
 41 ology for forward modeling in geodynamics and seismology. Lastly, we introduce melt
 42 migration dynamics beneath Réunion island, to which we applied our methodology.

43 1.1 Inverse vs. forward problems in geoscience

44 A multidisciplinary approach of exploration of the Earth's interior using seismology
 45 could be expressed as in Figure 1. The classic procedure (light blue arrows in Figure 1)
 46 starts from the collection of the seismic raw waveforms \mathbf{d} (see Equation 1). We then filter
 47 the observed waveforms and/or extract secondary information such as traveltimes, surface-
 48 wave phase velocity, receiver function, etc. We then invert these filtered data linearly, or
 49 in a linearized fashion (e.g. seismic tomography, full-wave waveform inversion), in order
 50 to obtain an inverted seismological model in terms of density, (an)isotropic seismic ve-
 51 locity and seismic attenuation. We then interpret the ensemble of seismic parameters as
 52 geodynamically meaningful parameters such as temperature and chemical anomalies in-
 53 side the Earth's mantle, based primarily on petrological knowledge. The geodynamicists
 54 will finally seek the most probable scenario(s) of the Earth's inner evolution, in order to
 55 qualitatively match their "virtual Earth models" to the tomographic "observation". This
 56 workflow (light blue arrows in Figure 1, expressed mathematically as eq. A.1 within Ap-
 57 pendix 1) is unavoidable when we do not have sufficient data or *a priori* information on
 58 the Earth's evolution [French and Romanowicz, 2015; Marjanović *et al.*, 2017].

59 Nevertheless, due to the regularization terms imposed throughout the chain of (lo-
 60 calized and) linearized inversions, it is difficult to quantitatively discuss the probability
 61 of proposed Earth's evolution scenarios[Ritsema *et al.*, 2007; Atkins *et al.*, 2016]. The
 62 only way to self-consistently answer this question is to directly model the full problem
 63 from first principles, and compare the predicted data with the real data: *i.e.* predict a self-
 64 consistent thermo-chemical structure, then predict the seismic properties, and subsequently
 65 make a full comparison with the observation. Here the observation is the seismic signal
 66 received at the Earth's surface. Following this methodology, we must perform every pro-
 67 cedure in a forward manner, and we propose that this approach is more powerful and ob-

68 jective than a series of inversions, in particular when we have geodynamical parameters \mathbf{m}
 69 to investigate (see Equation 1).

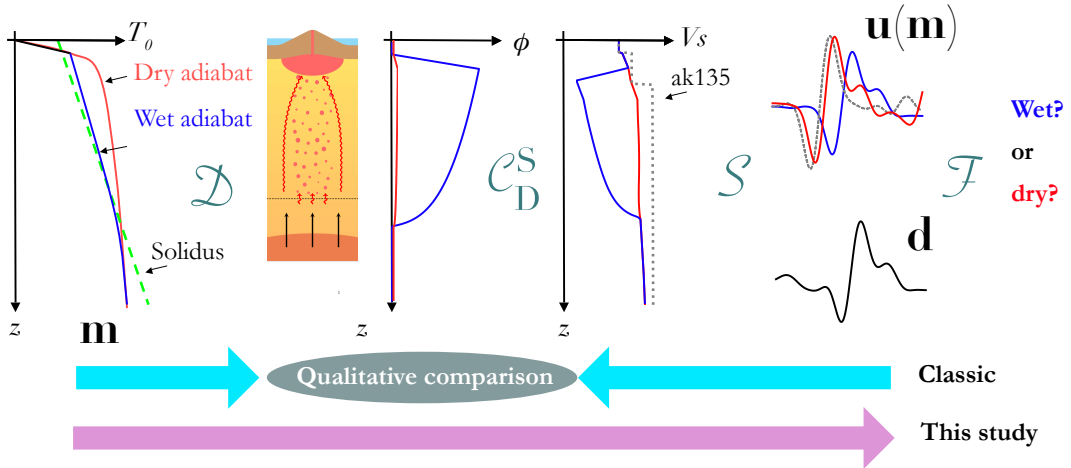
70 When we have a concrete set of geodynamical parameters to explore (e.g. degree
 71 of contribution of chemical heterogeneity to mantle convection or melt retention beneath
 72 a volcanic island, as in this paper), we should be able to directly, and quantitatively, in-
 73 vestigate the appropriateness of each ensemble parameter range, \mathbf{m} , against the observed
 74 seismic waveforms, \mathbf{d} , (Eq. 1). The crucial element to realize this direct comparison is re-
 75 lying on the capacity of forward modeling. Therefore, we propose to find the direct link
 76 between \mathbf{m} and \mathbf{d} by a series of forward modeling,

$$\mathbf{u} = \mathcal{S} \circ C_D^S \circ \mathcal{D}(\mathbf{m}), \quad (1)$$

77 with \mathbf{u} the “seismically (low-)filtered waveform data” instead of “seismically filtered model”
 78 (see the discussion in the appendix section). The operators \mathcal{D} , C_D^S , and \mathcal{S} , denote forward-
 79 modeling operators in geodynamics, petrology, and seismology, respectively (see the de-
 80 tailed discussion in Appendix 1). Due to the series of forward operators, the sensitivity
 81 of \mathbf{u} with respect to \mathbf{m} should be reduced: we therefore insist that this operation is “low-
 82 filtering”. The aim is thus to maximize the sensitivity by choosing a set of attributes from
 83 \mathbf{u} . The operation *per se* could be costly with respect to a series of inversions, but we can
 84 ideally perform a global search instead of local search. As indicated in the red arrow in
 85 Figure 1, we will be able to directly compare these “seismically (low-)filtered waveform
 86 data”, $\mathbf{u}(\mathbf{m})$, as a function of geodynamical model parameters, \mathbf{m} , and the observed data,
 87 \mathbf{d} .

98 1.2 Melt migration dynamics beneath the volcanic regions

99 For our first attempt to perform “waveform (low-) seismic filtering” (eq. 1 and eq. A.8
 100 in Appendix 1), we choose the melt migration dynamics beneath the volcanic regions.
 101 Within the Earth’s interior, melting most likely occurs only at the uppermost and lower-
 102 most mantle, due to the possible crossings of the mantle rock solidus and the geotherm
 103 [Karato, 2014; Herzberg *et al.*, 2013]. Within the asthenosphere below mid-ocean ridges,
 104 such as the East Pacific Rise (EPR), a seismic low velocity zone (LVZ) is found at depths
 105 between approximately 80 and 200 km with several percent of reduction in shear-wave ve-
 106 locity. The origin of such LVZs has been proposed to be due to the presence of partial
 107 melt [Stixrude and Lithgow-Bertelloni, 2005]. Direct comparison with experimental results



88 **Figure 1.** Conceptual schema of our waveform seismic filtering strategy (pink arrow for corresponding
 89 workflow). On the top from the left to right: we first generate (\mathcal{D}) geodynamical scenarios with different ini-
 90 tial conditions \mathbf{m} (T_0 for example: wet and dry in blue and red, respectively) in order to obtain a steady-state
 91 snapshot (vertical variation of porosity ϕ for example). We then translate (C_D^S) the set of geodynamical pa-
 92 rameters such as ϕ to a set of seismological parameters such as V_S . We then generate (\mathcal{S}) seismic waveforms
 93 \mathbf{u} to investigate the sensitivity of \mathbf{u} with respect to \mathbf{m} . We define a filter \mathcal{F} that can distinguish the different
 94 scenarios \mathbf{m} : we then analyze the observed data \mathbf{d} to select the preferred geodynamical scenario(s). Classical
 95 approaches (light blue arrows) try to fit the intermediate parameter sets such as seismic velocity structure or
 96 porosity structure that has unknown error bars due to a series of inversion procedures. A detailed discussion
 97 can be found in Appendix 1.

on rock assemblies of solid olivine and molten basalt infer small amounts of partial melt at 0.1 to 0.3 wt% levels [Chantel *et al.*, 2016]. Also, high melt transportation velocities (20 m yr^{-1}) at mid-ocean ridges are proposed based on U-series isotope study [Elliott and Spiegelman, 2003; Stracke *et al.*, 2006]. Yet, 2D geodynamical modeling together with a linear estimation on poroelastic effects of partial melt on shear-wave velocity requires a high melt retention (~0.3-2%) to explain the cause of LVZ obtained from surface-wave tomography at East Pacific Rise.

The EPR is one of the most studied and well understood areas of mantle upwelling and magma generation. Seismic observations from the MELT and GLIMPSE experiments at the EPR register a large negative velocity anomaly at the expected depth interval of the primary melting zone [Forsyth, 1998]. Based on S-wave travel time delay and Rayleigh wave phase velocity variations, there is an estimated 1-2% of melt present at this interval [Forsyth, 1998]. The low seismic velocities modeled below the EPR can not be replicated with a classic thermal model, that only considers conductive cooling [Harmon *et al.*, 2009]. This leads to the conclusion that there must be an additional reduction in seismic velocity due to the presence of at least 1% melt, taking the reduction in seismic velocity extrapolated from laboratory experiments [Hammond and Humphreys, 2000].

The question of the quantity of melt retained in the asthenosphere becomes more complicated if attenuation is included [Goes *et al.*, 2012]. The base of the LVZ below the EPR is at close to 100 km depth [Harmon *et al.*, 2009]. For significant melting to occur at this depth, the solidus needs to be lowered due to increased volatile content (e.g. Hirschmann *et al.* [1999]). The removal of volatiles as they partition into the deep melt will create a region of low- V_S and low- Q_S (high attenuation) that coincides with this deep melting [Goes *et al.*, 2012]. Volatile rich melting is however not productive, and no more than 0.1% melt is typically retained within the asthenosphere at depths between 200 and 90 km [Hirschmann *et al.*, 2009]. It is only within the shallow region (<60 km) of silicate melting that larger quantities of melt can be retained [Goes *et al.*, 2012]. This shallow region of low- V_S due to melt retention is un-resolvable at the resolution of the MELT and GLIMPSE experiments, therefore it can be concluded that the LVZ below the EPR is most likely due to the effects of attenuation and not melt retention.

Below volcanic islands such as Hawaii and the Galapagoes, a deep seismic discontinuity has been imaged at depths of 140 to 100 km [Rychert *et al.*, 2013, 2014]. This

140 seismic discontinuity is imaged in the form of S-to-P receiver functions, and has been in-
141 terpreted to represent the onset of deep volatile rich melting [Rychert *et al.*, 2013, 2014].
142 However, this interpretation is incompatible with forward models of melt generation and
143 transport [Havlin and Parmentier, 2014; Armitage *et al.*, 2015]. It was found that the only
144 way to generate a strong seismic discontinuity that could be imaged through S-to-P re-
145 ceiver functions is if the mantle contains no volatiles [Havlin and Parmentier, 2014]. Under
146 such conditions, the rate of melt production is sufficiently high to create a sudden step
147 in porosity, that would significantly reduce seismic velocities.

148 At regions of continental break-up, the same arguments of low- V_S and deep S-to-
149 P receiver functions have been used to argue for a significant quantity of melt retention
150 (e.g. Rychert *et al.* [2012]). However, just as before, forward geodynamic models have
151 been incapable of matching the tomographic models obtained using seismic inversions.
152 By modeling the composition and volume of melt generated in the Afar region of the East
153 African Ridge, it was found that melt retention in the asthenosphere was most likely no
154 more than 0.5 % [Armitage *et al.*, 2015]. In general, along the Afar Rift, forward models
155 have found that the magnitude of the observed seismic velocities can be explained without
156 the need for more than 1% melt retention [Armitage *et al.*, 2018, 2015].

157 Seismic studies consistently infer roughly 1 to 2% melt retention based on for ex-
158 ample the reduction in S-wave velocity below the East Pacific Rise (e.g. Harmon *et al.*
159 [2009]), seismic attenuation at the Juan de Fuca and Gorda ridges [Eilon and Abers, 2017],
160 or to generate the seismic discontinuity observed at the lithosphere - asthenosphere bound-
161 ary (LAB) in the central Atlantic [Mehouachi and Singh, 2018]. There is therefore clearly
162 a disconnect between what forward geodynamic models predict for melt retention (< 1 %)
163 and the quantity seismic interpretation calls for (> 1 %). In order to solve this enigma, we
164 propose a series of forward modeling both in geodynamics and in seismology, analyzing
165 one-station teleseismic data at Réunion island to understand the LVZ (of ~4%) based on
166 the partial melt hypothesis. We attempt to predict the observation, the seismic waveform,
167 from the structure predicted by the forward geodynamic model. We will focus on Réunion
168 given that previous studies indicate that this region likely contains some degree of melt
169 within the asthenosphere [Mazzullo *et al.*, 2017]. We predict the melt porosity and velocity
170 in a 1D upwelling mantle regime, and calculate the corresponding transport velocity of the
171 melt towards the surface. From the 1D model of temperature, pressure and melt fraction
172 we predict V_p and V_S velocities, and use these to generate synthetic waveforms across a

range of plausible mantle conditions. Finally, we integrate seismic observations from the Réunion mantle plume for a comparison with the synthetic seismograms to attain a best fit model in order to constrain mantle permeabilities, melt fractions and melt flow velocities below Réunion island.

1.3 Réunion island

In this study, we work on the 1D melt dynamics beneath the Réunion island. A recent surface wave seismic tomography model shows evidence for a 4% reduction in S-wave velocity at depths of around 80 km [Mazzullo *et al.*, 2017]. This could be indicative of high mantle temperatures and high degrees of melt retention. It is clear that the mantle is melting below La Réunion, but how much is retained within the mantle and contributes to the low velocities found within seismic inversions is unclear.

The first signature of plume activity in the western Indian Ocean dates back to 65–66 Ma in the late Cretaceous during the formation of the Deccan Traps, a large igneous province covering 500,000 km² [Duncan and Hargraves, 1990; Courtillot *et al.*, 2003]. The ascent of a deep mantle plume and its interaction with the base of the lithosphere, inducing surface volcanism and the formation of the Deccan Traps, is postulated as the beginning of the Réunion hotspot track [Richards *et al.*, 1989]. North-eastward plate movement of the African Plate 34 Ma ago created a linear chain of age-progressive islands, forming the Mascarene Plateau, Mauritius, and Réunion. This large oceanic volcanic system is located 800 km east of Madagascar and lies in the southernmost part of the Mascarene Basin. It is therefore assumed that the present day volcanic activity at the Piton de la Fournaise volcano on Réunion island is the surface expression of the upwelling mantle plume, and that there is a large quantity of melt being generated and transported to the surface below this volcanic island.

The petrology and geochemistry of the Piton de la Fournaise lavas can provide information on upper mantle conditions from which they originate, such as the thermal state at formation [Herzberg *et al.*, 2007]. As mantle convection drives mantle rock to the surface, fusible components of the peridotitic mantle rock melt at grain boundaries when solidus temperature and pressure conditions are reached. The residual solid matrix becomes a porous medium for fluid flow, where buoyant forces arise from a density differential between the liquid melt and solid matrix, and drive melt towards the surface. Although the

composition of the melt may be modified during its ascent by fractional crystallization and/or mixing, lava samples can be reconstructed into their primary magma composition from which the MgO content can be used as an indicator of source temperature. Concentrations of MgO are predominantly temperature dependent, meaning magmas with a high MgO content reflect dry and hot source conditions [Hirose and Kushiro, 1993]. Geochemical analysis of primary magmas from Réunion formations show high MgO concentrations of 16-20 wt %, indicating melting conditions of mantle peridotites at temperatures above 1450 °C [Sobolev and Nikogosian, 1994]. Furthermore, a ~ 2 km thick underplated magmatic body deduced from receiver function inversions and seismic refraction profiles [Fontaine et al., 2015; Charvis et al., 1999; Gallart et al., 1999] has been proposed to consist of ultramafic primary melt originating from 60-90 km depths [Richards et al., 2013].

A high temperature upper mantle below Réunion is in line with local seismic tomography studies which confirm a low shear wave velocity zone (LVZ) below the oceanic crust [Fontaine et al., 2015; Mazzullo et al., 2017]. The LVZ phenomenon is not unique to Réunion, but has been observed globally below hotspots, rifts and mid-ocean ridges in areas such as Afar, the East Pacific Rise, Hawaii, the Galapagos and Iceland. There is abundant evidence for partial melting associated to deep mantle upwelling in these areas. However, the quantity of partial melt and its significance to LVZ remain contested by geodynamic, seismic, and petrologic studies: are these LVZ's purely thermal or require an additional mechanism, such as the presence of partial melt (e.g. Goes et al. [2012]; Eilon and Abers [2017]; Cobden et al. [2018])? The dynamics of the system and the mechanisms responsible for the velocity anomaly remaining poorly understood, other explanations involving upper mantle anisotropy, attenuation, volatile content, solid state mineralogy, and grain boundary sliding are still being explored.

2 Methods

How much melt can be retained in LVZ? Or, more in general, what is the cause of LVZ and its role in whole mantle convection? As we discussed in the introduction, we propose a series of forward modeling through geodynamics, petrology and seismology, in order to understand the sensitivity of geodynamical parameters to the seismic observations. Seismic inversion studies of the structure beneath the Réunion island have provided valuable results on the quantification of low shear-wave velocity zones. Here, our forward modeling approach will allow us to control individual model parameters in geodynamics instead of

seismic parameters (see the discussion in the Appendix), in order to test their effects directly on seismic observations: seismic waveforms themselves. We therefore develop a 1D melting model, which is converted to seismic velocities, density and attenuation, and then we propagate a seismic wave through models of a range of mantle conditions (eq. A.8). We explore the sensitivity of geodynamical scenarios to seismic attributes $\mathcal{F}(\mathbf{u})$ and analyze the observed seismic data to conclude. In particular in this study, it consists of the four unknowns:

$$\mathbf{m} = (k_0, T_0, \bar{v}, \phi)^T \quad (2)$$

with k_0 the permeability coefficient, T_0 the initial temperature, \bar{v} the average upwelling velocity and ϕ the porosity.

2.1 1D Geodynamical modeling

The production and transport of melt in the 1D melting system can be described by the following set of modified Stokes equations [McKenzie, 1984; Ribe, 1985]. We consider a 1D system where mantle moves upwards, and as it does so it decompresses and melts (Figure 1). The evolution of this system can be described by a set of continuum equations beginning with temperature. The temperature of the system over time is described by a general advection-diffusion equation that incorporates melting as a source term:

$$mL + \rho c \frac{\partial T}{\partial t} + \rho c \bar{v} \frac{\partial T}{\partial z} - \kappa \frac{\partial^2 T}{\partial z^2} = 0 \quad (3)$$

where m is the melt production rate, L the latent heat of melting, ρ the density, c the specific heat capacity, T the temperature, \bar{v} the average upwelling velocity, z the system depth in kilometers and κ the heat conductivity.

The average upwelling velocity consists of a solid and a liquid upwelling component, with the mantle rock matrix being the solid and the melt as the liquid component:

$$\bar{v} = (1 - \phi)v_s + \phi v_l, \quad (4)$$

where v_s and v_l are (respectively) the velocity of the upwelling matrix and melt and ϕ is the porosity.

Melting of the upwelling mantle rock occurs when its temperature and pressure conditions exceed that of the solidus (Figure 1), which we assume is only a linear function of pressure and is given by:

$$T_s = T_{s0} + \frac{\partial T_s}{\partial p} p \quad (5)$$

where $T_{s0} = 1080^\circ\text{C}$ and $\frac{\partial T_s}{\partial p} = 132 \times 10^{-9} \text{ }^\circ\text{C Pa}^{-1}$ [Scott, 1992]. We assume melt production rate m is governed by the difference in mantle temperature T and solidus temperature T_s , $\Delta T = T - T_s$, the latent heat L from melting, and a depletion term $\partial T_s / \partial \phi$ that accounts for the increased difficulty to melt depleted mantle:

$$m = \Delta T \left(L + \frac{\partial T_s}{\partial \phi} \right)^{-1}. \quad (6)$$

The depletion term is generally controlled by mantle composition, where melting becomes more difficult as pyroxenes and clinopyroxenes are extracted from the solid mantle into the melt and the less fusible olivine remains (e.g. Morgan [2001]). However, since mantle composition is not directly implemented into the 1D model, we approximate depletion using a power law relation:

$$\frac{\partial T_s}{\partial \phi} = C e^{a\phi} \quad (7)$$

where $C = 440 \text{ K}$ is a constant for the initial depletion value [Morgan, 2001] and $a = 5.5$ is a dimensionless depletion coefficient that we use to create a diminishing melt production. Note that C has a dimension of temperature since porosity is dimensionless. This simplified set of melting relations does not capture the full complexities of multi-component melting (e.g. Morgan [2001]; Katz *et al.* [2003]). It does however capture the most important aspects of melt generation to allow for a 1D melt transport model, and give a simple model solution through which to propagate seismic waves.

The melt transport through the system is approximated as the flow of a liquid phase through a porous medium, which is described by Darcy flow. To create a set of closed equations we need to approximate for the relationship between permeability and porosity as follows:

$$k_\phi = k_0 \phi^n, \quad (8)$$

where k_ϕ is the permeability and k_0 is the permeability coefficient, with k_0 and n being constants empirically derived from experiments. At grain-scale melt distributions in partially molten olivine basalts n has been empirically determined to be approximately equal to 2.7 for melt fractions of $\phi > 0.02$ [Miller *et al.*, 2014]. The constant k_0 is much more uncertain, with estimates of mantle permeability k_ϕ ranging from 10^{-15} m^2 to 10^{-10} m^2 (e.g. Burley and Katz [2015]), k_0 is between $\sim 10^{-5} \text{ m}^2$ to 10^{-10} m^2 , assuming $n = 3$. Taking the above closure equation in 8, the flow of the melt, v_l is subsequently given by:

$$\phi(v_l - v_s) = \frac{k_0 \phi^n}{\eta_l} \left(\Delta \rho g + \frac{\partial}{\partial z} p \right) \quad (9)$$

where the term $\Delta\rho g + \partial p/\partial z$ describes the potential gradient which drives the flow, where $\Delta\rho$ is the density difference between fluid and matrix, g the acceleration due to gravity, and $\partial p/\partial z$ the pressure gradient due to compression of the matrix.

A zero compaction length approximation is adopted, which assumes no contribution of matrix compaction to porous flow. The matrix compression term in eq. 9 can be neglected if melt flow is one dimensional and the length scale over which melting occurs is much larger than the reduced compaction length δ_R defined as follows [Ribe, 1985]:

$$\delta_R = \left[\frac{\phi_0 \bar{v} (\zeta_s + \frac{4\eta_s}{3})}{g \Delta\rho} \right] \quad (10)$$

with ζ_s and η_s respectively the bulk and shear viscosity of the solid matrix and ϕ_0 a reference porosity. Assuming ζ_s and $\eta_s = 10^{15} - 10^{18}$ Pa s [e.g. Ribe, 1985], $\Delta\rho = 500$ kg m⁻³ [e.g. Hewitt, 2010] and the reference porosity an estimated range of $\phi_0 = 0.1 - 5$ % we determine an average reduced compaction length for the 1D melting model at 5 – 50 m, with a maximum upper boundary of 5000 m for model extremities. The height of the melting column is approximately 80 km, which is three to four magnitudes larger than our estimated reduced compaction length.

We adopt a Boussinesq approximation for the density ρ , where the density of solid matrix and melt are equivalent except in the buoyancy term [Hewitt, 2010]. The conservation of mass for melt is given by:

$$\rho \frac{\partial \phi}{\partial t} + \rho \frac{\partial}{\partial z} \phi v_l = m. \quad (11)$$

Under the assumption of a zero compaction length and assuming $n = 3$, Darcy's equation (eq. 9) can be written as,

$$\phi (v_l - v_s) = \frac{k_0 \phi^3}{\eta_l} (\Delta\rho g) \quad (12)$$

To get a solvable equation for melt velocity we incorporate eq. 4 in eq. 12, and then substitute this into eq. 11 to get a set of equations for melt production and transport as function of porosity:

$$\rho \frac{\partial \phi}{\partial t} + \rho \bar{v} \frac{\partial \phi}{\partial z} + \frac{k_0 \Delta\rho g}{\eta_l} \frac{\partial}{\partial z} [\phi^3 (1 - \phi)] = m. \quad (13)$$

Here \bar{v} is the imposed upward velocity of the melt and solid matrix, and ϕ is therefore the only unknown and it therefore can be solved numerically.

313 2.2 Numerical method for melt production and transport

314 The 1D partial melting model computes temperature as a function of depth and time
 315 through the general advection-diffusion equation (eq. 3, eq. 13), discretized using Crank-
 316 Nicolson method. At the depth of 410 km we initialize the initial mantle temperature (T_0)
 317 as a fixed temperature boundary condition. At the surface temperature is fixed at 0 °C.
 318 The model has 410 evenly spaced grid points from 410 km depth to the surface of the
 319 Earth. Once the temperature of the system exceeds solidus temperature T_s , the finite dif-
 320 ference scheme determines the production of melt as a function of previous depletion, re-
 321 calculating temperature according to latent heat from melting for each time step according
 322 to eq. 6. The third term in eq. 13 can be expressed as an advection term $q \frac{\partial \phi}{\partial z}$ where:

$$323 q = \frac{k_0 \Delta \rho g}{\eta_l} \left[3\phi^2 \left(1 - \frac{4}{3}\phi \right) \right], \quad (14)$$

324 giving a scheme for calculating ϕ in the next time-step as:

$$325 \phi_j^{l+1} = \phi_j^l - \frac{\bar{v}q(\phi_j^l - \phi_{j-1}^l)}{\Delta z}, \quad (15)$$

326 where superscript l are the points in time and subscripts j the points in space. The free
 327 parameters that we will explore are mantle temperature, upwelling velocity, and the per-
 328 meability coefficient k_0 . Models are run until a steady state is achieved. The melt flow
 329 velocity, temperature, and melt production as a function of depth are calculated for a range
 330 of scenarios variable upwelling velocities of \bar{v} (10 – 70 mm yr⁻¹), initial temperatures of T_0
 331 (1250 – 1500 °C), and permeability coefficients of k_0 (10⁻⁹–10⁻⁵ m²), at increments of re-
 332 spectively 10 mm yr⁻¹, 50 °C and a factor 10, giving 210 different model scenarios. These
 333 parameter ranges describe a series of feasible geodynamic conditions in mantle plume en-
 334 vironments.

335 2.3 Conversion to seismic properties

336 At the Earth's surface we cannot directly "see" the melt retention calculated in the
 337 previous section, but only the geochemical or seismological observations. In this study
 338 we intend to analyze the sensitivity of seismic waveforms with respect to the melt re-
 339 tention. We therefore construct seismological models from geodynamical modeling con-
 ducted beforehand. To realize this idea, temperature, pressure, and porosity are converted
 to isotropic P- and S-wave velocities.

To compute seismic velocities for the geodynamical 1D models, we follow the methods of *Goes et al.* [2012]. Phase diagrams and anharmonic velocities are computed using Perplex [Connolly, 2005], and the equation of state, solid solution models and 2008-NaCFMAS mineral parameter data base of Sixtrude and co-workers [*Stixrude and Lithgow-Bertelloni, 2005; Xu et al., 2008*]. Subsequently we assume attenuation is given by [*Cammarano et al., 2003; Goes et al., 2012*]:

$$Q = A\omega^\alpha \exp\left(\frac{\alpha\gamma T_s}{T}\right). \quad (16)$$

This Arrhenius style attenuation relationship is empirical, where the melting temperature T_s is used as an alternative to estimating the depth dependence on activation volume [Karato, 1993]. The constants are $A = 0.1$, $\alpha = 0.15$, and $\gamma = 38$, and we set $\omega = 2\pi/20.0$ (with a dominant period of 20 s). Since we use large band-pass filters from 100 s to 5 s and apply a frequency-independent attenuation during our synthetic seismogram computation, we used this *ad hoc* value in order that the attenuation remains in the range of $\pm 20\%$ of Arrhenius attenuation described above for all the frequencies. The anharmonic velocity and anelastic contributions are subsequently combined to give the seismic velocity [*Goes et al., 2012*]:

$$V = V_{\text{anh}} \left[1 - \frac{Q^{-1}}{2 \tan(\pi\alpha/2)} \right]. \quad (17)$$

Finally, to include the effect of melt we follow a convention of a 3.6% and 7.9% velocity reduction per percent melt for respectively the P- and S-wave velocities according to *Hammond and Humphreys* [2000], where the velocity derivatives are based on an organized cuspatate pore geometry with relaxed elastic moduli to model a maximum possible effect of melt on seismic wave velocity. Teleseismic waves excite the relaxed modulus of partially molten upper mantle rock, and therefore we assume relaxed, pressure equilibrated melt conditions when relating seismic velocity reduction to the mantle physical state [*Hammond and Humphreys, 2000*].

Wave velocities at depths below 410 km are set to *ak135* [*Kennett et al., 1995*], since the mineral database only covers the upper mantle up to the Moho. We assume no percolation of melt into the crust and set the model porosity to 0% at the Moho to crudely simulate extraction for simplicity purposes. This is somewhat artificial as there will be a degree of melt storage within the crust in the form of sills and melt lenses. However, it is beyond the scope of the 1D model developed here to examine these processes. Given the wavelength of seismic waves used to probe the structure of the lithosphere and as-

thenosphere to understand melt retention, we believe this region can be assumed to be similar to *ak135*. An artifact from this approximation might be a sharp porosity discontinuity at the top of the LVZ, which is modified into a more gradual porosity transition as seen from observations to avoid overestimation of the impedance contrast during synthetic waveform generation. Perceived from seismic tomography results from the Réunion mantle plume, the LVZ starts at about 27 km depth, and reaches a minimum velocity at 32 km depth [Fontaine *et al.*, 2015]. We apply a moving average filter over this depth range to smooth the top of the porosity curve. The bottom of the model space is truncated at 410 km depth to coincide with the the 410-discontinuity in *ak135* reference model.

379 2.4 Seismological modeling

380 In order to compute full-wave synthetic seismograms for a number of given 1-D
 381 Earth models in this study up to as high frequency as 1 Hz, we use Direct Solution Method
 382 [Geller and Ohminato, 1994; Geller and Takeuchi, 1995; Kawai *et al.*, 2006]. The DSM
 383 obtains the solution of the weak form of the equation of motion by directly solving the
 384 Galerkin weak form of the equation of motion:

$$(384) \quad (\omega^2 \mathbf{T} - \mathbf{H}) \mathbf{c} = -\mathbf{g},$$

385 with ω the angular frequency, \mathbf{T} and \mathbf{H} the mass and stiffness matrices, respectively. \mathbf{g} is
 386 the external force vector and \mathbf{c} is the expansion coefficient of the displacement. We choose
 387 the spherical harmonics along the lateral directions of the Earth and linear spline along
 388 the vertical direction for basis and trial function expansion of all the vectors and matrices
 389 described above. This finite element formulation adheres to natural boundary condition
 390 (free surface boundary) and fluid-solid boundary conditions. Numerical dispersion due
 391 to the discretization can successfully be eliminated through implementation of optimally
 392 accurate operators [Geller and Takeuchi, 1995]. The ellipticity of the Earth is also taken
 393 into account. The reader can refer to the literature cited herein for further theory and the
 394 extension of DSM to 3D Earth models can be found in [Cummins *et al.*, 1997; Fuji *et al.*,
 395 2012; Monteiller *et al.*, 2015].

396 The reference Earth model we use for DSM consists of 1D *ak135* model [Kennett
 397 *et al.*, 1995]. By embedding velocity profiles from our converted models into the reference
 398 model at the 12-410 km depth range, we generate different sets of synthetics for several
 399 source events while varying upper mantle temperatures, upwelling velocities and perme-

abilities. The time window is set to a length of 3276.8 s to include surface waves at high offset source events, in order to avoid numerical artifacts from superimposition of surface wave energy out of the time window. We calculate seismograms up to 0.3125 Hz so that we can filter them up to 0.2 Hz to compare against the observed waveforms. It is worth noting here that DSM naturally prefers a time window of 0.1 s times a power of 2 in order for the inverse Fourier transform to be free from numerical errors. In this study we consider only isotropic homogeneous media since we will analyze teleseismic phases up-going through the melt conduit beneath Réunion island.

408 3 Seismological data

409 We would like to extract the geodynamical information from the direct observation
 410 on the Earth's surface. Unlike current seismic tomography that makes use of a tremen-
 411 dous amount of data, we would like to extract as much information as possible from a
 412 small number of data (21 earthquakes with only one seismic station in Réunion island) to
 413 detect signatures from differences in geodynamical scenarios within each individual seis-
 414 mological datum. In this study we will initially focus on the sensitivities of different com-
 415 binations of permeability, temperature and upwelling velocity on the synthetic waveform.
 416 Furthermore, we compare the synthetic seismograms for each source event with seismic
 417 observations acquired from Réunion. The synthetics are generated using DSM according
 418 to source and receiver configurations of the seismic observations of the Réunion mantle
 419 plume in order to place the models in the context of the Earth.

420 3.1 Receiver

421 Earthquake observation data are obtained from the GEOSCOPE Observatory, a
 422 global network of broadband seismic stations transmitting real-time seismic data to the
 423 Institute de Physique du Globe de Paris (IPGP) data center, from which the data is man-
 424 aged and distributed [Douet *et al.*, 2016]. It comprises of a network of 34 seismological
 425 stations in 18 different countries, and offers a catalog of earthquakes registered between
 426 2006 and 2018 with magnitudes above 5.5-6. All stations are equipped with three broad-
 427 band seismometers type STS1 or a 3-component seismometer type STS2, a digitizer, and a
 428 local storage system for the data [Douet *et al.*, 2016].

436

Table 1. Receiver information RER GEOSCOPE seismic station

Receiver	Latitude (degrees)	Longitude (degrees)	Elevation (m)	Channels	Sampling Rate (Hz)
GEOSCOPE RER	-21.17	155.74	834	BHZ, BHN, BHE	20

429

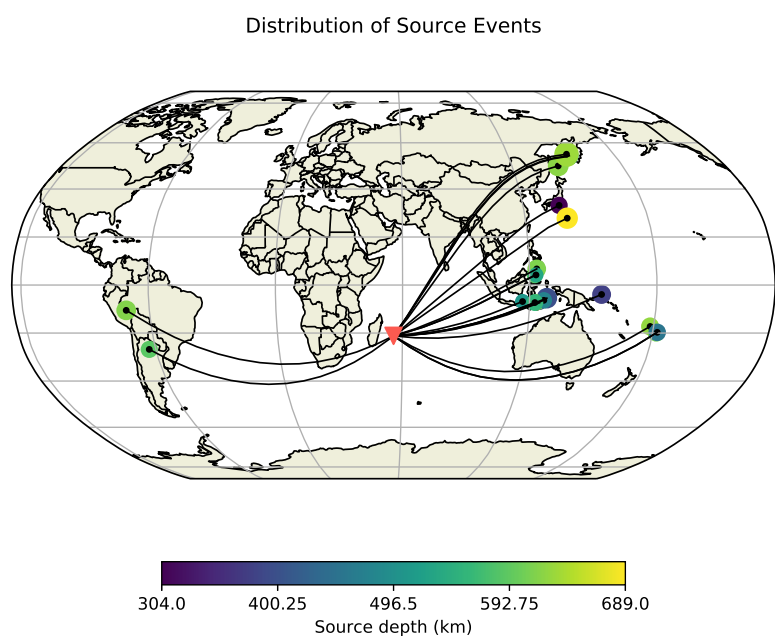
Seismic data is acquired from the GEOSCOPE RER seismic station (table 1), which is part of the GEOSCOPE Observatory network. This seismic station is situated directly above the upwelling plume on top of the Piton de la Fournaise volcano, capturing seismic waves that have traveled through the LVZ that should contain information on the melting zone. Table 1 contains the receiver specifications for the RER receiver. The seismic observations of interest are recorded as time series data on the broadband seismometer channels of the RER station.

437

3.2 Seismic sources

438

From the entire earthquake catalog registered at the RER GEOSCOPE station between January 2006 and December 2015 a selection of events is used for synthetic waveform generation. The selection criteria to decide on adequate source events are based on their source depth, epicentral distance from RER station, signal-to-noise ratio and clarity of the phase arrivals. To avoid seismic interaction with potential upper-mantle and crustal interfaces and/or melting at the source location, we select deep earthquakes with a source depth greater than 300 km so that the upper mantle effects for observed and synthetic seismograms are only on the RER station-side. We ensure teleseismic incidence at the receiver location by selecting source events at epicentral distances at least beyond 30 degrees [Bormann and Wielandt, 2002]. The epicentral distance range of the seismic sources used in this study is from 60 to 120 degrees. In order for an automated waveform correlation to function, we require relatively high signal-to-noise ratio and high amplitude P and S phase arrivals up to a level where the signal is not masked by noise. Source half duration time should not exceed the period at which it has been band-pass filtered since the synthetics are simulated with a Heavyside source time function, that we will convolve with the source time function provided by SCARDEC (see section 4.2). Table 2 displays the seismic events from the RER GEOSCOPE catalog which satisfy all the criteria.



457 **Figure 2.** Geographical distribution of source events (table 2). Depth is displayed by color and earthquake
458 magnitude by size of the circular markers. The location of the RER GEOSCOPE receiver is marked by a red
459 inverted triangle.

455 **Table 2.** List of 21 events used in our analyses. Half Duration times (HD) have been taken from Global
 456 CMT.

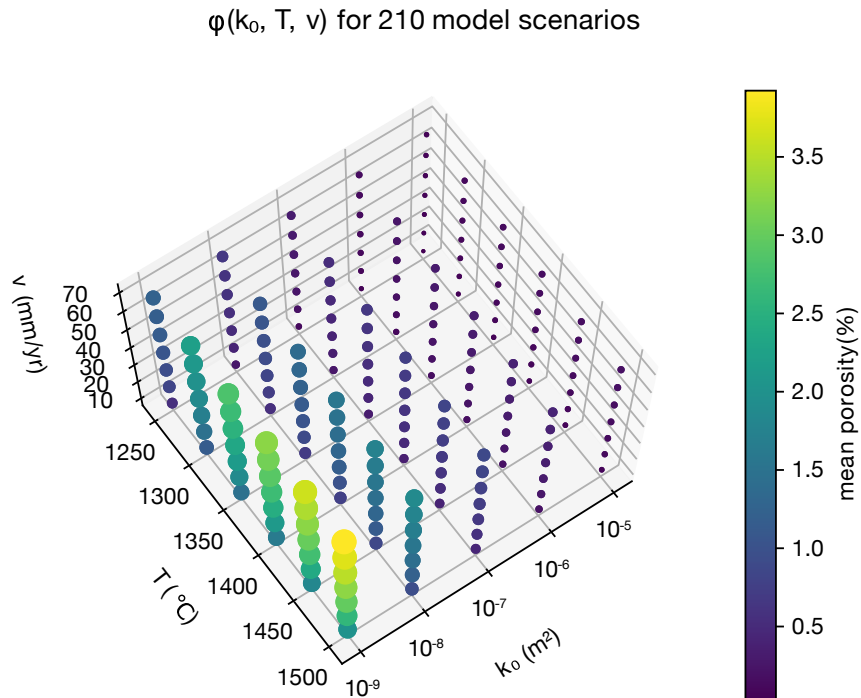
#	Source Event	Date (yyyy/mm/dd)	Time (h:m:s)	Latitude (degrees)	Longitude (degrees)	Epicentral dist. (degrees)	Depth (km)	Magnitude	HD (s)
1	Bali Sea	2011/03/10	17:08:36	-6.87	116.72	60.51	510	6.6	4.8
2	Fiji Islands	2006/01/02	22:13:40	-19.93	-178.18	113.15	609	7.1	9.3
3	Banda Sea	2006/01/27	16:58:53	-5.47	128.13	71.62	397	7.7	16.0
4	Sea of Okhotsk	2008/07/05	02:12:04	53.88	152.89	111.11	636	7.7	17.3
5	Sea of Okhotsk	2008/11/24	09:02:58	54.2	154.32	111.98	518	7.3	10.9
6	Banda Sea	2008/12/06	10:55:26	-7.39	124.75	67.81	404	6.5	3.9
7	Honshu	2009/08/09	10:55:55	33.17	137.94	95.26	304	7.0	8.3
8	Banda Sea	2009/08/28	01:51:20	-7.15	123.43	66.66	633	6.9	6.8
9	Celebes Sea	2009/10/07	21:41:13	4.08	122.37	69.92	587	6.8	5.9
10	Fiji Islands	2009/11/09	10:44:55	-17.24	178.33	111.88	626	7.2	10.5
11	Mindanao	2010/07/23	22:08:11	6.72	123.41	71.96	615	7.3	11.0
12	Santiago Del Estero	2011/01/01	09:56:58	-26.8	-63.14	103.84	590	7.0	8.0
13	Celebes Sea	2011/02/10	14:39:27	4.2	122.97	70.52	533	6.6	4.5
14	Banda Sea	2011/08/30	06:57:41	-6.36	126.75	70.03	476	6.9	6.7
15	Sea of Okhotsk	2012/08/14	02:59:38	49.8	145.06	105.59	622	7.7	17.8
16	Sea of Okhotsk	2013/05/24	05:44:49	54.9	153.28	111.46	632	8.3	35.7
17	New Ireland	2013/07/07	18:35:30	-3.92	153.92	96.18	379	7.4	10.9
18	Fiji Islands	2014/11/01	18:57:22	-19.69	-177.76	113.61	455	7.1	8.7
19	Flores Sea	2015/02/27	13:45:5	-7.297	122.54	65.77	557	7.0	7.5
20	Bonin Islands	2015/05/30	11:23:02	27.84	140.49	95.35	689	7.8	20.7
21	Peru-Brazil Region	2015/11/24	22:45:38	-10.54	-70.94	118.79	617	7.5	16.6

460 **3.3 Data processing**

461 Seismic observations acquired from the RER station are deconvolved with the instru-
 462 ment response of the receiver before being subjected to further processing. Hereafter, the
 463 north and east horizontal components seismograms are rotated respectively along and per-
 464 pendicular to the great circle path into their radial and transverse components in order to
 465 separate the P-SV waves from SH waves.

466 Both the synthetics and seismic observations are subjected to a band-pass filter, ex-
 467 ploring upper corner frequencies of 0.05 Hz to 0.2 Hz (i.e. lowest periods of 20 s to 5 s)
 468 with a lower bound kept constant at 0.01 Hz (i.e. 100 s). At frequencies beyond 0.2 Hz
 469 the automated cross-correlation algorithm that compares wave arrivals becomes unsta-
 470 ble due to increasing discrepancies related to short-wavelength structure. This automated
 471 comparison between synthetic and observed data is set up through automated phase pick-
 472 ing and time window selection. The cross-correlation time window is chosen based on
 473 three factors: i) the maximum band-pass frequency, where the smallest wavelength is
 474 determined through Nyquist theorem; ii) windowing range is set to be a quarter of the
 475 dominant period; and iii) a trailing window to account for variation throughout all source
 476 events. The precursor is essential to capture a length of flat signal foregoing the phase ar-
 477 rivel, which significantly improves distinction between the phase arrival and any arbitrary
 478 sinusoidal signal. The trailing windows have been empirically set to 10 s for P-waves, 20 s
 479 for S-waves, and are predominantly required to account for variation in wavelengths be-
 480 tween source events and waveform widening caused by high melt models.

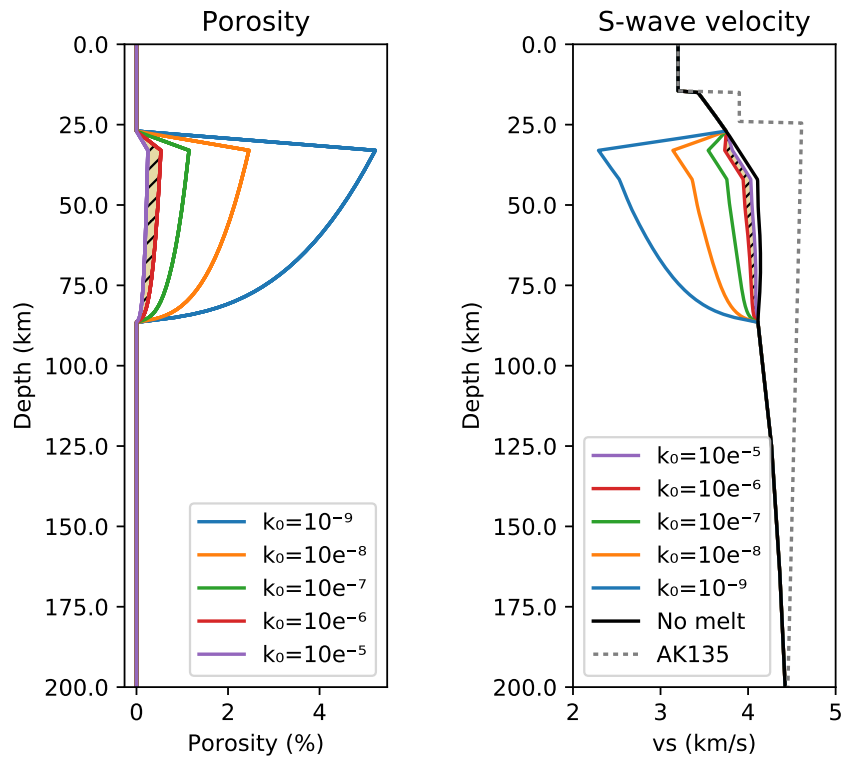
481 Phase picking is initiated through TauP method [Buland and Chapman, 1983; Crotwell
 482 *et al.*, 1999], in order to compute theoretical travel time arrivals for each seismic phase
 483 for a given earth model. TauP enables us to center the cross-correlation time window on
 484 a given phase of the *ak135* synthetic trace. We proceed to find the time shift between
 485 this phase in *ak135* and the presumed phase arrival in the data traces and all synthetic
 486 model traces by cross-correlating the two traces. The time-shift is used to shift the cross-
 487 correlation window to the phase arrivals for each seismic and synthetic trace, allowing
 488 for comparison of phase arrivals between data and models in order to find seismic travel
 489 time delay $t_{P,S}^{\text{shift}}$. We compute the differential travel time between the P and S arrival for
 490 both the observed seismic trace and synthetic trace, and define the residual between the
 491 two as $t_{S-P}^{\text{obs,syn}}$. Since melt affects seismic velocity reduction for P and S waves differently,
 492 matching the inter-phase differential travel time of the observed waveforms with the mod-
 493 els can help to put a constraint on porosity. Although phase arrivals vary in time with
 494 source depth and epicentral distance, we find that relative time travel differences between
 495 synthetic and observed traces, such as $t_{P,S}^{\text{shift}}$ and $t_{S-P}^{\text{obs,syn}}$, are insensitive to varying source
 496 depth between 300-700 km and are virtually unaffected by changes in epicentral distance
 497 at the offsets used in this study (~0.001-0.01 s decrease per degree).

498 **4 Results**499 **4.1 1D melting model**

500 **Figure 3.** The geodynamic model scenarios considered in this study are represented by scatterpoints for
 501 each combination of the free parameters $k_0 = 10^{-9}-10^{-5} \text{ m}^2$, $T_0 = 1250-1500 \text{ }^\circ\text{C}$ and $\bar{v} = 10 - 70 \text{ mm yr}^{-1}$,
 502 giving a total of 210 model scenarios. The mean porosity for each model scenario is illustrated by both scatter
 503 color and size.

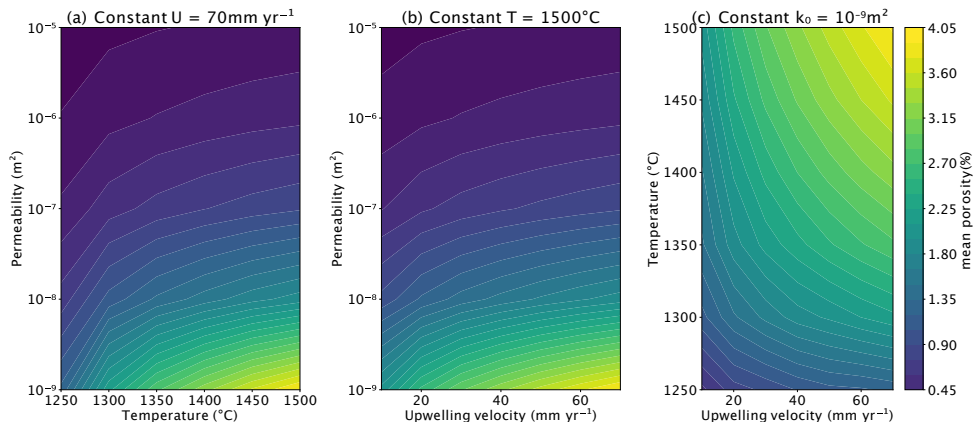
511 The melting model calculates porosity and the depth profile of temperature for all
 512 combinations of the free parameters explored in Figure 3, resulting in 210 geodynamic
 513 model scenarios. For each model scenario the model temperature, pressure and porosity
 514 as a function of depth are converted to seismic wave velocity according to section 2.3.
 515 Seismic wave velocities reduce gradually with reducing depth due to a general decrease
 516 in density and the increasing attenuation of the seismic wave due to temperature effects
 517 [Goes *et al.*, 2012]. At pressure-temperature conditions above the solidus the presence of
 518 melt reduces seismic wave velocity in line with the empirical velocity reduction taken
 519 from *Hammond and Humphreys* [2000]. As a result the models with lower permeabil-

Model scenarios: $T=1450\text{ }^{\circ}\text{C}$, $v=70\text{ mm/yr}$



504 **Figure 4.** Porosity and S-wave velocity as a function of depth for the range of permeability coefficients
 505 explored in figure 3, with temperature and the upwelling rate fixed at respectively $1450\text{ }^{\circ}\text{C}$ and 70 mm yr^{-1} .
 506 The velocity profile for the *ak135* reference model is shown in gray, and velocity profile for a model without
 507 melt is shown in black. The hashed area between the porosity and velocity profiles indicate the most probable
 508 model obtained during our “waveform filtering” inversions for the partial melting beneath Réunion island
 509 according to this study. At 30 km depth melt is assumed to leave the system, as here it is probable that the
 510 porous flow is no longer a valid assumption for the transport of melt.

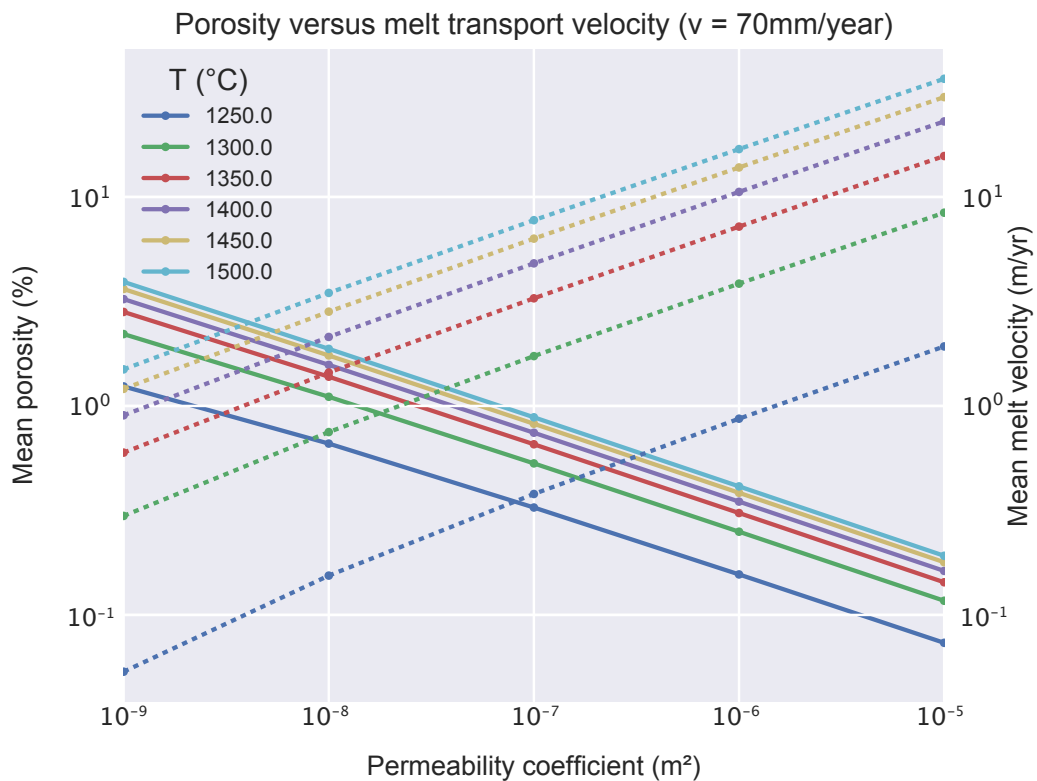
520 ity coefficients that create greater melt retention have a larger reduction in seismic wave
 521 velocity (Figure 4). We take an example case of a basal temperature of 1450 °C and up-
 522 welling rate of 70 mm yr⁻¹ to describe the modeled vertical porosity and the generated
 523 seismic velocity profiles (Figure 4). The depth of the initiation of melting is predomi-
 524 nantly controlled by temperature, and lies at roughly 85 km if the basal temperature is
 525 fixed at 1450 °C. Lower temperatures will yield a shallower onset of melting. Depend-
 526 ing on the assumed permeability, the onset of melting can be marked by a sharp increase
 527 in porosity. In particular, if the permeability is low, say, when $k_0 = 10^{-9}$ m², a porosity
 528 greater than 2% can be rapidly achieved under these conditions (Figure 4). This is equiva-
 529 lent to a permeability of 8×10^{-15} m² in eq. 8. At the other end of spectrum, if we assume
 530 a high permeability $k_0 = 10^{-5}$ m², porosity is between 0.1 and 0.5%, which means that
 531 permeability is between 10^{-14} m² and 10^{-12} m². This range of permeability is within the
 532 range or higher than those experimentally observed in high-temperature high-pressure ex-
 533 periments (e.g. 10^{-16} m² for a porosity of 2% [Miller *et al.*, 2014] or 10^{-14} m² for a poros-
 534 ity of 5% [Connolly *et al.*, 2009]).



535 **Figure 5.** Development of porosity over full range of input parameters k_0 , T and \bar{v} . (a) Temperature
 536 vs. permeability coefficient at a constant upwelling velocity of 70 mm yr⁻¹. (b) Upwelling velocity vs. per-
 537 meability coefficient at a constant temperature of 1500 °C. (c) Upwelling velocity vs. temperature at a con-
 538 stant permeability coefficient of 10^{-9} m².

539 If we compare the mean porosity from the range of input parameters, we find that
 540 in general the assumed permeability coefficient has the most dominant role in controlling
 541 retained melt volumes, over initial temperature and upwelling velocity (Figure 5). The lat-
 542 ter two parameters appear to have an approximately linear effect on melt porosity, with

543 temperature being the more controlling parameter of the two, according to the contour
 544 gradients between Figure 5a and 5b, and the dominating horizontal trend in Figure 5c.
 545 We observe a slight increased melt production gradient with temperature from slight nar-
 546 rowing in vertical contour spacing in Figure 5a. However, change in porosity is largely
 547 driven by permeability coefficient. The smaller the permeability coefficient, the larger the
 548 porosity, which can be found in narrowing of the contours in Figure 5a and 5b.



549 **Figure 6.** Logarithmic plot of the variation in modeled porosity (solid) and melt flow velocity (dashed) with
 550 permeability coefficient and temperature, with upwelling velocity constant at 70 mm yr^{-1} . The relationship
 551 between porosity and mean melt flow velocity is inversely proportional as a function of the permeability
 552 coefficient, and proportional as a function of temperature.

553 Over the tested permeability range the mean porosity ranges from 3.92% at the min-
 554 imum permeability case to 0.03% at the maximum permeability case (Figure 6). The
 555 minimum and maximum mean melt transport velocity values over our input range are
 556 respectively 0.011 m yr^{-1} at minimum permeability and temperature, and 36.77 m yr^{-1}
 557 at maximum permeability and temperature, with a local velocity maximum peaking at

558 90.98 m yr⁻¹ for the maximum. Melt flow velocity is inversely proportional to melt porosity as a function of k_0 (Figure 6; *Weatherley and Katz* [2016]). This is because the increased connectivity enhances the flow of melt, allowing for higher melt flow velocities.
 559
 560
 561 Melt is extracted and transported to the surface more rapidly, resulting in a lower retention of melt at the onset of melting. Hence, more efficient removal of melt avoids melt
 562 accumulation, decreasing maximum porosity with the increase of permeability. U-series
 563 disequilibrium studies constrain melt flow velocities at $\sim 20 - 50$ m yr⁻¹ from short lived
 564 ^{266}Ra excesses [*Elliott and Spiegelman*, 2003; *Stracke et al.*, 2006]. Melt velocities of such
 565 magnitude point towards high permeability coefficients ($k_0 = 10^{-6} - 10^{-5}$ m²), which
 566 would mean low melt porosity below 0.3% and permeability of 10⁻¹⁴ m².
 567

568 4.2 Synthetic Seismograms

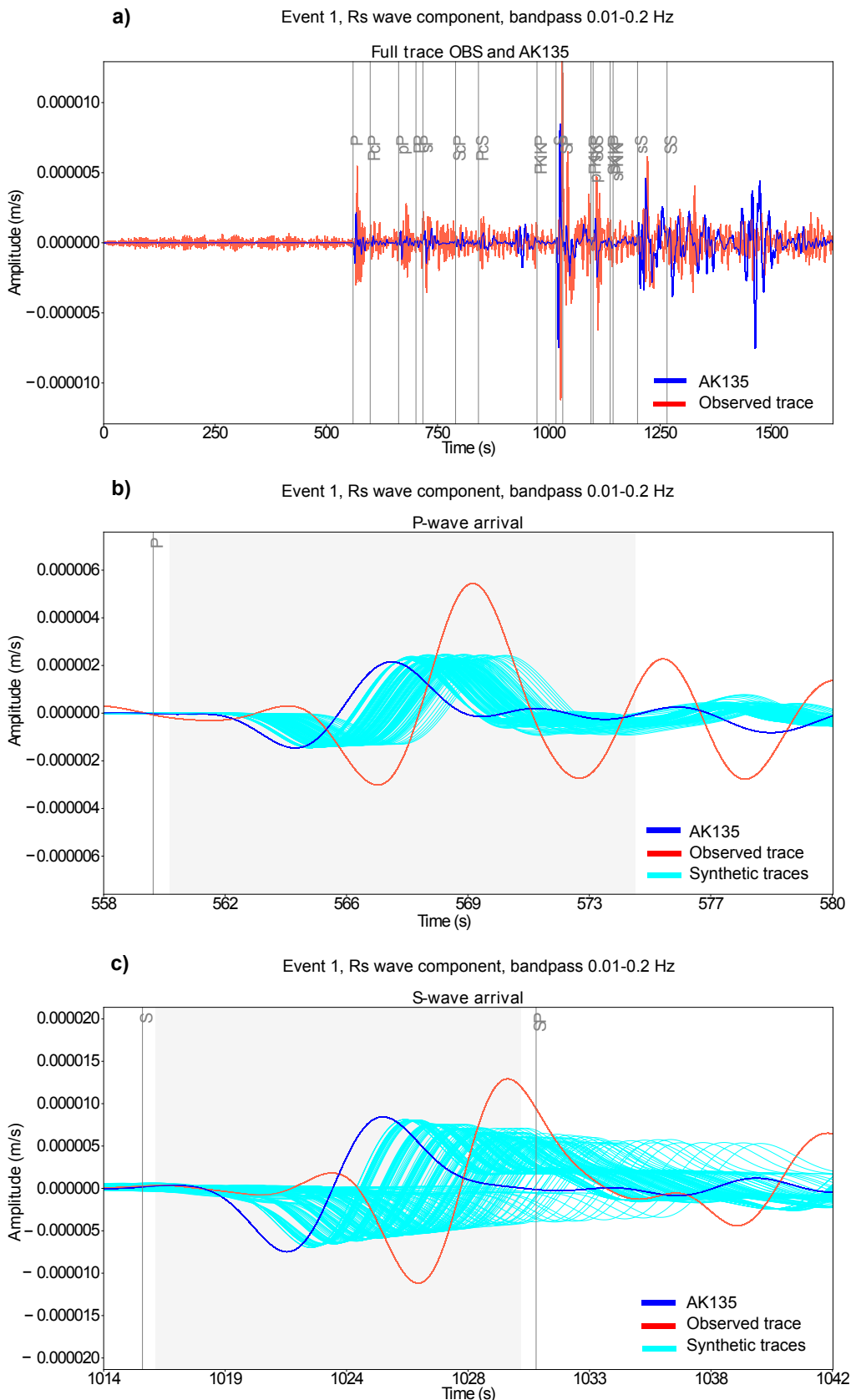
569 For all 21 source events listed in Table 2 we generate synthetic seismograms. The
 570 source adopts the moment tensor of the respective event and is propagated through the
 571 range of 1D models for the different mantle temperatures, upwelling velocities, and per-
 572 meability coefficients, resulting in 210 sets of seismograms per source event (recall Fig-
 573 ure 5). The synthetics are convolved with the source-time function of their respective
 574 source event, since DSM uses a delta function as its moment-rate function. Source-time
 575 functions for each source event were acquired through the SCARDEC source time func-
 576 tions database [*Vallée and Douet*, 2016]. Convolution with the source-time function will
 577 adjust phase arrivals in time. For source events with a half-duration time higher than the
 578 band-pass filtering frequency period, convolution with the source-time function will be
 579 especially important for accurate prediction of the observed waveforms.

580 In the upcoming synthetic waveform analysis we focus on the P-wave and S-wave
 581 arrivals or the Pdiff and SKS phase arrivals, depending on the epicentral distance of the
 582 respective event. The epicentral distances between sources and receiver range from 60 de-
 583 grees to 120 degrees. At epicentral distances beyond 100 degrees P-waves are no longer
 584 direct, but begin to diffract along the core-mantle boundary and are registered as a Pdiff
 585 phase. Similarly, S-waves are also no longer direct beyond a 100 degrees epicentral dis-
 586 tance as well, however we find that in the epicentral distance range of 100-120 degrees
 587 the SKS phase experiences less interference with other phases and has higher amplitude
 588 arrivals than the Sdiff phase for source events at 300-700 km depth.

589 During synthetic waveform analysis we investigate four different frequency bands.
 590 Waveforms are band-pass filtered from 0.01 Hz to upper limits of 0.05 Hz, 0.1 Hz, 0.15 Hz
 591 and 0.2 Hz.

597 For each considered event, phase arrival and wave component, the 210 synthetic
 598 models (Figure 7) are cross-correlated with the seismic observation to find the time shift
 599 between the two traces. Travel time delay $t_{P,S}^{\text{shift}}$ of the model with the observation is plot-
 600 ted against the inter-phase differential travel time $t_{S-P}^{\text{obs,syn}}$ in order to constrain model sce-
 601 narios in time (Figure 8). In most cases, the travel time delay and differential travel time
 602 do not line up at 0 simultaneously, giving a range of likely model scenarios in between
 603 $|t_{S-P}^{\text{obs,syn}}|$ at $t_{P,S}^{\text{shift}} = 0$, and $|t_{P,S}^{\text{shift}}|$ at $t_{S-P}^{\text{obs,syn}} = 0$. We define the best-fit models for a given
 604 phase arrival by simultaneously minimizing $|t_{P,S}^{\text{shift}}|$ and $|t_{S-P}^{\text{obs,syn}}|$ through minimizing the
 605 combined quadratic mean (RMS) of the two variables (Figure 8). The RMS will be min-
 606 imal for instances where $|t_{P,S}^{\text{shift}}|$ and $|t_{S-P}^{\text{obs,syn}}|$ are equal, which is preferable since the two
 607 variables are inherently coupled, where the inability to match one of them is related to the
 608 other.

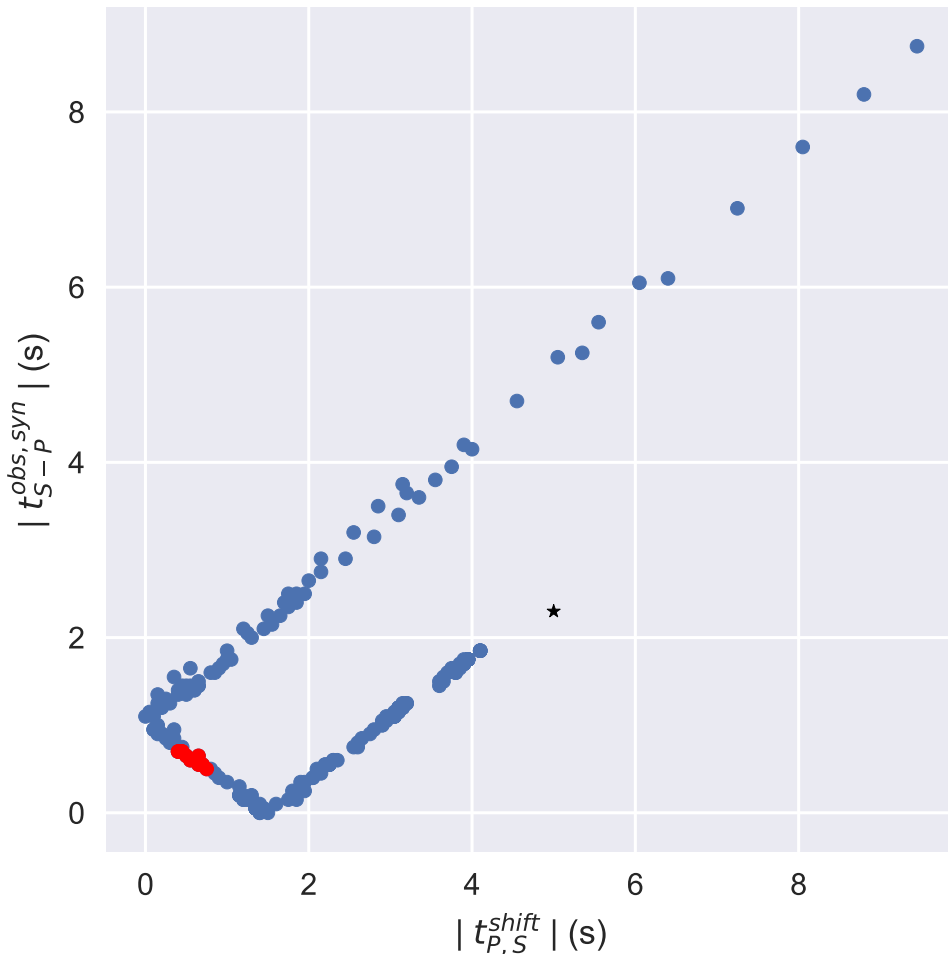
612 Additional quality checking was conducted during the picking of best-fit model sce-
 613 narios among all sets of events, phases, components and band-pass filter bandwidths. Sets
 614 are removed if the models deviate from the expected pattern displayed (red points in Fig-
 615 ure 8), which means that cross correlation between observation and models has failed to
 616 identify the correct arrival. Automated cross correlation of seismic phases is a sensitive
 617 process that is prone to failure if the circumstances are not close to ideal. If the observed
 618 signal does not possess a high signal-to-noise ratio, clear and high amplitude phase ar-
 619 rivals, a distinct source-time function and all together a high similarity with the synthetic
 620 trace, cross-correlation is not guaranteed to work accurately. Cross-correlations at band-
 621 pass filter bandwidths of 0.01 – 0.05Hz performed poorly and were omitted in their en-
 622 tirety, whereas cross-correlations for the other frequency bands tend to improve with in-
 623 creasing frequency. From the initial 21 source events only 12 events passed the quality
 624 check. A majority of the excluded sources are high offset events with epicentral distances
 625 greater than 110°.



592 **Figure 7.** a) Seismogram containing the radial components of the full synthetic waveform generated for
 593 *ak135* base model (blue) and the observed seismic trace (red) for event 1, band-pass filtered from 0.01 to
 594 0.2Hz. b) A close-up of the P-wave arrival of trace presented in a), with the additional 210 synthetic traces
 595 (light blue) generated for our melting models. The gray zone represents the automated cross-correlation
 596 window used to find the time shift with the observed trace. c) The equivalent of b) for the S-wave arrival.
 -27-

Relative travel times between observed and synthetic traces

Event 1: S-wave Rs component

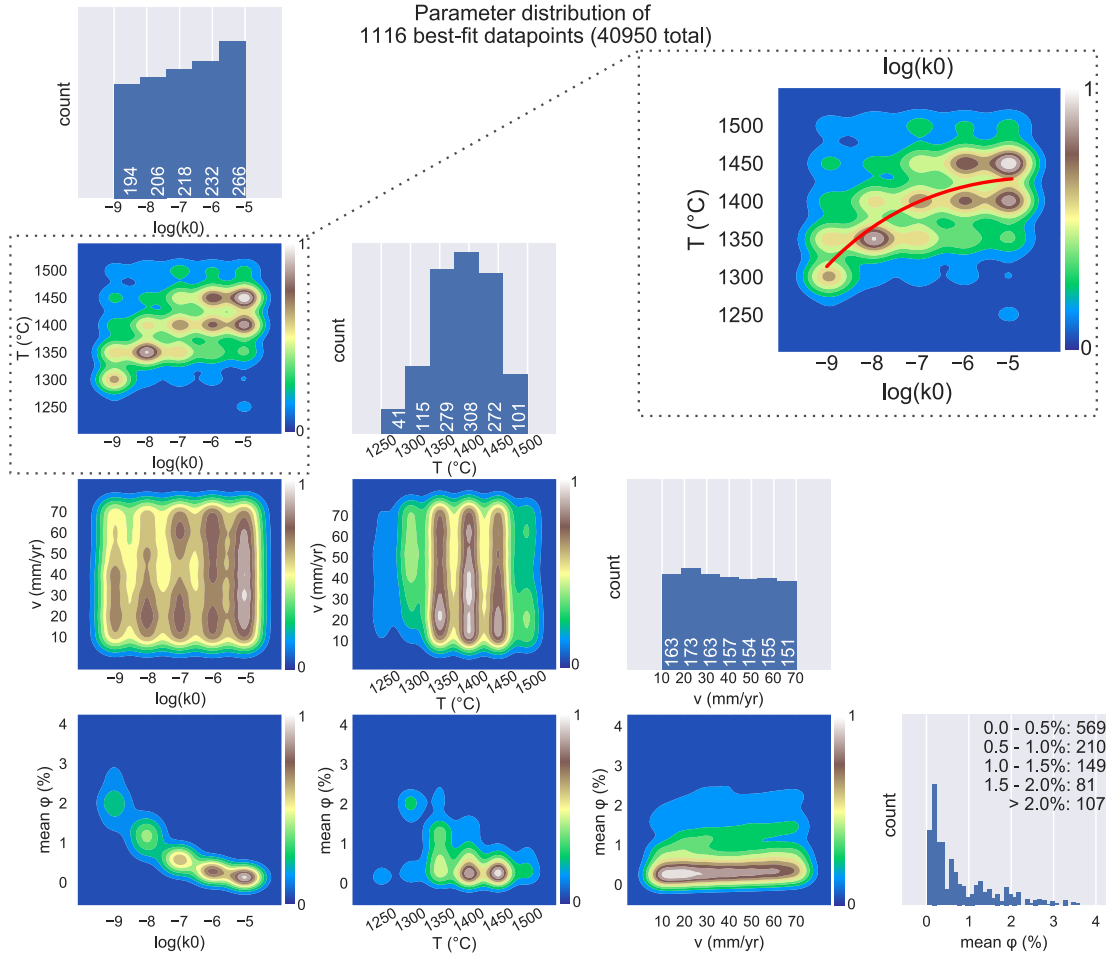


609 **Figure 8.** Plotting the absolute value of the travel time delay $|t_{P,S}^{\text{shift}}|$ versus the absolute value of the differ-
 610 ential travel time $|t_{S-P}^{\text{obs,syn}}|$ for the radial component of the S-wave arrival from the Bali Sea earthquake. Best
 611 fit models by minimized RMS are displayed in red, whereas results for *ak135* are presented by a black star.

626 **4.3 Comparison against seismological observations**

627 In order to discover which modeled melting scenario describes the upper mantle be-
 628 low Réunion most adequately, we will analyze the distribution of best-fit scenarios among
 629 the free model parameters k_0 , T and \bar{v} for the remaining source events that passed quality
 630 checking. The best fit conditions are, however, non unique solutions, since the porosity we
 631 aim to constrain is a function of all three input parameters. Certain trade-offs between k_0 ,
 632 T and \bar{v} will have the same outcome in porosity.

643 By cross-correlating synthetic traces for 210 model scenarios with the seismic ob-
 644 servation for 12 source events, compiled for 4 phase arrivals (P, S, Pdiff, SKS), 3 wave
 645 components (Rs, Ts, Zs) and all the band-pass filter frequencies (upper corner frequencies
 646 of 0.05, 0.1, 0.15 and 0.2 Hz) we conducted a total 70,896 synthetic to observed phase
 647 comparisons, of which we consider 40,950 cases where cross-correlation between phases
 648 was successful. From these 40,950 cases there were 1116 best matches in time between
 649 observed and synthetic waveforms, which form a distribution around the most probable
 650 model scenario to describe the upper mantle beneath Réunion among the 210 model sce-
 651 narios. The changes in porosity caused by alterations in upwelling velocity are too in-
 652 significant to constrain a specific value of \bar{v} , and all values of \bar{v} are equally represented for
 653 the entire range of temperatures and permeability coefficients (Figure 9). The results indi-
 654 cate that most best-fit scenarios are covered by the temperature range of 1350 – 1450 °C.
 655 There is a gradual preference to higher permeabilities, although all permeability coeffi-
 656 cients are covered. That is because the time delay is a product of melt, which is largely
 657 controlled by the permeability coefficient, and the intrinsic anelasticity that increases with
 658 temperature. For each permeability there is a temperature counterpart which will result in
 659 a similar travel time delay. High temperatures are coupled with high permeability coeffi-
 660 cients, where the travel time delay is dominated by temperature attenuation. On the other
 661 hand there are the melt dominated cases where low temperatures are coupled with low
 662 permeabilities. The $T-k_0$ relationship in Figure 9 suggests that permeability coefficients of
 663 $k_0 = 10^{-9} \text{ m}^2$ are generally coupled with $T = 1300 \text{ }^\circ\text{C}$, $k_0 = 10^{-8} \text{ m}^2$ with $T = 1350 \text{ }^\circ\text{C}$,
 664 $k_0 = 10^{-7} \text{ m}^2$ with $T = 1350 - 1400 \text{ }^\circ\text{C}$, $k_0 = 10^{-6} \text{ m}^2$ with $T = 1400 - 1450 \text{ }^\circ\text{C}$ and
 665 $k_0 = 10^{-5} \text{ m}^2$ also with $T = 1400 - 1450 \text{ }^\circ\text{C}$. At higher permeabilities the tempera-
 666 ture regimes become indistinguishable because the melt percentages are so low that the
 667 travel time delay is dominated by the effect of temperature. These five clusters make up
 668 the possible conditions in the upper mantle below Réunion that can explain our chosen set



633 **Figure 9.** Pair grid plot displaying the distribution of permeability coefficient k_0 , basal temperature T ,
 634 upwelling velocity \bar{v} and mean melt porosity ϕ among the 1116 best-fit traveltimes options out of 40950 data
 635 points (2.7% of the dataset with highest fit). Histograms on the diagonal count the representation of values for
 636 the variables k_0 , T , \bar{v} and ϕ among 1116 data points that have minimized $t_{P,S}^{\text{shift}}$ and $t_{S-P}^{\text{obs,syn}}$ with the observed
 637 traces. The off-diagonals show contour plots setting each of the input variables against each other, highlighting
 638 certain values within variable pairings that give a minimized solution to matching seismic travel times.
 639 The color scale shows relative density between minimum count and maximum count of the values for the
 640 variables in question, indicating which combination of values for any two variables are most likely to give a
 641 best-fit solution. Plotting temperature versus permeability coefficient shows the relationship between T and k_0
 642 in red for which relative travel times are minimized.

of seismic observations. The mean melt porosity for each cluster is with increasing permeability coefficient respectively 1.88%, 1.11%, 0.58%, 0.29% and 0.13%. Depending on the upper mantle temperature each of these melt scenarios is a viable solution. The data suggests the most likely temperature is 1400 – 1450 °C, based on the combined number of matches with $k_0 = 10^{-5} – 10^{-6}\text{m}^2$ with respect to the number of other matches. Secondly, the mean travel time delay and mean differential travel time for each cluster is minimal for $k_0 = 10^{-6} – 10^{-5}\text{m}^2$ at $t_{P,S}^{\text{shift}} = 0.06 \pm 0.51\text{ s}$ and $t_{S-P}^{\text{obs,syn}} = -0.20 \pm 0.46\text{ s}$, supporting a mantle temperature of $T = 1400 – 1450\text{ }^\circ\text{C}$. Under these conditions we can expect porosity of maximum 0.28.

5 Discussion

In this study, we proposed a series of forward modeling from geodynamical modeling to seismic waveform computation (eq. A.8). Instead of collecting a big dataset, we first settled the geodynamical parameters to explore (eq. 2). The consequences are that we were able to generate seismological models $C_D^S \circ \mathcal{D}\mathbf{m}$ that are geodynamically consistent. Hereafter, we discuss our results in detail.

The data suggest that the most likely temperature conditions in the upper mantle beneath Réunion are $T = 1400 – 1450\text{ }^\circ\text{C}$, with permeability coefficients in the range of $k_0 = 10^{-5} – 10^{-6}\text{m}^2$. Equally minimizing $t_{P,S}^{\text{shift}}$ and $t_{S-P}^{\text{obs,syn}}$ through RMS has corrected for not being able to solve for the relative arrivals of the P- and S-waves, and the position in time of the entire wave packet simultaneously. This gives more distinction in the temperature space, while losing some contrast along the permeability coefficients, because the effect of temperature on P and S wave velocities is close to linear and therefore has little effect on inter-phase differential travel times. This makes it a better measure of the position in time of the wave packet as a whole. If, on the other hand, we put 100% weight on $t_{S-P}^{\text{obs,syn}}$ then we lose some constraint on fitting the entire wave packet in time, but tighten the constraints on the relative travel time difference between phase arrivals. This in turn gives better distinction along the k_0 range at the expense of T , because predominantly the permeability coefficient controls inter-phase differential travel times. Both cases emphasize the favored scenarios of $T = 1400 – 1450\text{ }^\circ\text{C}$ and $k_0 = 10^{-5} – 10^{-6}\text{m}^2$. Regardless of the weighting used for $t_{P,S}^{\text{shift}}$ and $t_{S-P}^{\text{obs,syn}}$ during the minimization process of the best-fit scenarios, the outcome remains robust despite slight redistribution of high temperatures and permeabilities.

Our predicted values for temperatures of $T = 1400 - 1450^\circ\text{C}$ approach potential mantle temperatures for the lower end of MgO values suggested for primary magmas from Réunion (16% *wt*) at 1440–1480 °C, according to calculations from the MELTS numerical algorithm [Ghiorso and Sack, 1995; Asimow *et al.*, 2001] and formulations of upper mantle potential temperatures [Herzberg *et al.*, 2007]. Temperature estimates from this study appear slightly too low to explain the full range of MgO values of up to 20% *wt* deduced from the Réunion transitional series, which indicate source temperatures up to 1650 °C [Sobolev and Nikogosian, 1994]. However, this could be the result of the idealized melt microstructures adopted in our models. When performing parameter conversion we assume a uniform network of organized cuspate melt pockets that induce maximum seismic velocity reduction per percent melt, respectively 3.6% and 7.9% for P and S waves in relaxed conditions [Hammond and Humphreys, 2000]. Other melt pocket geometries, such as ellipsoidal or tubular shaped pore spaces, sustain lower velocity reductions per percent melt, namely 2.1% and 4.3% for the former, and 1.2% and 2.7% for the latter for the P and S waves. If we consider a non-uniformly distributed combination of pore geometries instead, we can expect overall a slightly lower effect of melt porosity on seismic velocity reduction. As a consequence the best-fit scenarios will overcompensate either by reducing the permeability coefficient or increasing temperature to attain a minimized travel time delay. This will cause greater polarization across the potential scenarios between the low porosity (high T and k_0) and high porosity (low T and k_0) cases, for which we have better constraints for high temperature.

For the predicted temperature values the onset of melting is at 74.7–86.0 km depth for respectively $T = 1400 - 1450^\circ\text{C}$. This corresponds to a 60–90 km source depth for ultramafic melt that is proposed as origin of the ~2 km thick underplated body observed at the base of the crust (Richards, 2013), and possibly aligns with depth of the LAB [Fontaine *et al.*, 2015].

Values for the permeability coefficient predicted from the results for the upper mantle beneath Réunion are $k_0 = 10^{-6} - 10^{-5}\text{m}^2$, which translate to upper mantle permeabilities of $10^{-14} - 10^{-12}\text{m}^2$ calculated for a porosity range of 0.13 – 0.28%. Coefficients of 10^{-6}m^2 on average result in marginally better matches in time with the seismic observations, and are more in line with experimental results of permeability in high-temperature high-pressure environments, at coefficients of $2 \times 10^{-16}\text{m}^2$ to $5 \times 10^{-13}\text{m}^2$ for porosity between 0.02 – 0.2 [Connolly *et al.*, 2009]. The mean melt transportation velocity values

range in between $8.37 - 18.35 \text{ m yr}^{-1}$ for coefficients of respectively $k_0 = 10^{-6} - 10^{-5} \text{ m}^2$, approaching the lower melt flow rates of 20 m yr^{-1} suggested by Uranium isotope migration rates [Elliott and Spiegelman, 2003; Stracke *et al.*, 2006]. The model melt flow velocity could be higher if opting for a lower exponent n in the permeability-porosity relationship, where values down to 2 are within the accepted range for grain geometries in the upper mantle [Goes *et al.*, 2012; Zhu and Hirth, 2003]. By doing so the predicted permeabilities will decrease to $10^{-13} - 10^{-11} \text{ m}^2$ for $n = 2$, diverging from the earlier constraints put on permeability and only conceivable for coefficients of 10^{-6} m^2 .

Across all source events the mean travel time difference and differential travel time for the best-fit model scenarios with $T = 1400 - 1450^\circ\text{C}$ and $k_0 = 10^{-5} - 10^{-6} \text{ m}^2$ are $t_{P,S}^{\text{shift}} = 0.06 \pm 0.51 \text{ s}$ and $t_{S-P}^{\text{obs,syn}} = -0.20 \pm 0.46 \text{ s}$, since within the majority of source events $t_{P,S}^{\text{shift}}$ and $t_{S-P}^{\text{obs,syn}}$ do not simultaneously converge to 0 s. Overall the synthetic phase arrival is slightly too early (i.e. $t_{P,S}^{\text{shift}}$ is positive) with respect to the observed and therefore the inter-phase differential travel time is slightly wider (i.e. $t_{S-P}^{\text{obs,syn}}$ is negative). Adopting a less idealized melt microstructure network will improve convergence towards 0 s, as it will slightly reduce the P-to-S velocity reduction ratio induced by melt, and therefore reduce relative phase arrivals of compressional versus transverse waves. This relies on the assumption that the *ak135* reference model adequately approximates the geodynamical properties of the earth on a global scale, and that the slight travel time discrepancy is a result of our presumptions on the modeled effect of melt on seismic wave propagation. It is likely that along each raypath for the studied source events there are velocity anomalies with respect to the *ak135* reference model, that are captured in our results through the misalignment in the $t_{P,S}^{\text{shift}} - t_{S-P}^{\text{obs,syn}}$ relationship (Figure 8). The nature of the ratio between $|t_{P,S}^{\text{shift}}|$ at $t_{S-P}^{\text{obs,syn}} = 0$ and $|t_{S-P}^{\text{obs,syn}}|$ at $t_{P,S}^{\text{shift}} = 0 \text{ s}$ for each source event could tell something about the cause and magnitude of the velocity anomalies along the raypath. Furthermore, differences between the radial, transverse and vertical seismic wave components could give insights on anisotropy within the velocity anomalies. When $t_{S-P}^{\text{obs,syn}}$ does not converge to 0 s it suggests that relative velocities between P- and S-waves are altered through any other means than melt presence as defined in this study. Local scale heterogeneities such as lattice-preferred orientation of melt flow, shape preferred orientation of the pore geometry, crystalline anisotropy, or the presence of volatiles in the upper mantle could be relevant if there is notable heterogeneity along the raypaths between different seismic phases at seismic resolutions. When $t_{P,S}^{\text{shift}}$ does not converge to 0 s it indicates

767 that the wave packet as a whole is either early or late with respect to the observations,
 768 and could hint at large scale heterogeneities along the raypaths such as large low-shear-
 769 velocity provinces (LLSVP), ultra-low velocity zone (ULVZ) or mantle plumes. The gen-
 770 eral early phase arrival from the best-fit conditions could indicate a higher expected ve-
 771 locity anomaly from the Réunion mantle plume than modeled, but to identify the source
 772 would require extensive comparisons with tomographic cross-sections along the raypaths
 773 for each source event.

774 6 Conclusion

775 In this study, we proposed a series of forward modeling in geodynamics and seis-
 776 mology in order to understand the direct link between the geodynamical parameters and
 777 seismic observation. We developed a partial melting model for the upper mantle in order
 778 to model melt porosity for 210 different combinations of permeability coefficients, tem-
 779 perature and upwelling velocity. For each model scenario synthetic seismograms were
 780 generated for 21 source events using the Direct Solution method with the *ak135* refer-
 781 ence model as base model for global wave propagation. Analysis of travel time delay and
 782 inter-phase differential travel time of P, Pdiff, S and SKS phase arrivals between synthetic
 783 waveforms and observed traces recorded at the RER GEOSCOPE receiver at Réunion al-
 784 lows us to statistically constrain several local geodynamic conditions in the upper man-
 785 ttle. Our results indicate that we are unable to constrain upwelling velocity, but are able
 786 to constrain the most probable combination of temperature and permeability coefficient
 787 at $T = 1400 - 1450^{\circ}\text{C}$ and $k_0 = 10^{-5} - 10^{-6} \text{ m}^2$, which appear consistent with studies
 788 of potential mantle temperature based on MgO content. The proposed high permeabili-
 789 ties promote high rates of melt extraction at $8.37 - 18.35 \text{ m yr}^{-1}$, which is in accordance
 790 with results from Uranium isotope migration studies. Furthermore, from these predicted
 791 conditions follows that the onset of melting in the upper mantle beneath Réunion lies in
 792 between 74.7 – 86.0 km depth and most importantly that melt porosity does not exceed
 793 0.28 %.

794 Low velocity zones in the shallow upper mantle can be explained by a combina-
 795 tion of relatively high mantle temperatures and low percentages of melt retention, which
 796 go hand in hand with rapid melt extraction as a result of high permeability conditions in
 797 the melting zone. The results are able to satisfy prevalent geodynamical and geochemi-
 798 cal predictions of low melt retention and high melt flow rate, while simultaneously ade-

799 quately accounting for seismic data. We found that differences between travel time delay
800 and inter-phase differential travel time of the synthetic traces versus the observed wave-
801 forms can indicate velocity anomalies along the raypath with respect to the base model,
802 and could potentially tell something about their nature.

803 **Acknowledgments**

804 This work was funded by the ANR grant Interrift. Numerical computations were partly
805 performed on the S-CAPAD platform, IPGP, France. We acknowledge IRIS (Incorporated
806 Research Institutions for Seismology) data center for RER station data (<https://doi.org/10.7914/SN/IU>).
807 We also would like to thank Lapo Boschi, Saskia Goes, two anonymous reviewers and the
808 editors for their constructive comments. This is IPGP contribution XXXXX.

809 **A: Appendix: Inverse vs forward problems in geoscience**

810 A conceptual representation of the classical method for exploration of the Earth's
 811 interior inherent to inversion procedures could be written as follows:

$$\mathbf{m}_{\text{inv}} = \mathcal{D}^\dagger \circ C_S^D \circ (\mathcal{F}_{\text{comp}} \circ \mathcal{S})^\dagger \circ \mathcal{F}_{\text{obs}}(\mathbf{d}) \quad (\text{A.1})$$

812 where \mathbf{m}_{inv} is a vector of estimated geodynamical model parameters that we look for, \mathbf{d} a
 813 vector of seismic observed waveforms, with \mathcal{D} the geodynamical modeling operator, C_S^D
 814 parameter conversion operators from petrology to seismology, \mathcal{S} the seismic wave propa-
 815 gation operators and $\mathcal{F}_{\text{comp}}$ and \mathcal{F}_{obs} the seismic data processing operators applied to (or
 816 embedded in) computed data and observed data, respectively. All the operators above are
 817 essentially non-linear in nature (occasionally linear, especially the seismic modeling op-
 818 erator $\mathcal{F}_{\text{comp}} \circ \mathcal{S}$). † denotes “general inverse” of those operators. The reason why we
 819 precise the use of \mathcal{F} inside Eq. A.1 is our incapacity of modeling a whole series of seis-
 820 mic waveform data. When we measure only traveltimes $\mathcal{F}_{\text{obs}}(\mathbf{d})$ for instance, we use a
 821 linear Eikonal operator as $\mathcal{F}_{\text{comp}} \circ \mathcal{S}$. Indeed, due to the high frequency approximation of
 822 wave equations in Eikonal equation, $\mathcal{F}_{\text{comp}}$ can be different from \mathcal{F}_{obs} . Even wave-equation
 823 based expensive operators $\mathcal{F}_{\text{comp}} \circ \mathcal{S}$ [Komatitsch and Vilotte, 1998; Geller and Takeuchi,
 824 1998; Hasegawa *et al.*, 2018] are not an exception: the frequency contents and included
 825 physics will never meet the real Earth. Therefore, we have to (pre-)process the raw data \mathbf{d} .
 826 This discussion should be valid to some extent for other operators such as C and \mathcal{D} but
 827 for the simplicity we do not discuss it in this paper.

828 Eq. A.1 reads as follows:

- 829 (i) We collect the seismic raw waveforms \mathbf{d} from the existing stations.
- 830 (ii) We filter the waveforms, and/or picking traveltimes by cross-correlations or hand-
 831 picking of some phases of interest or surface-wave phase velocity picking, receiver
 832 function calculation, envelope calculation, or simply windowing of waveforms: we
 833 denote all the data processing symbolically as $\mathcal{F}_{\text{obs}}(\mathbf{d})$ to distinguish the raw wave-
 834 form data and the secondary seismic attributes to take into account.
- 835 (iii) Seismic inversion is then applied to the seismic attributes in order to infer the inner
 836 structure of the Earth in terms of density, (an)isotropic seismic velocity and seismic
 837 attenuation. This relies on the general inverse of forward modeling operators $\mathcal{F}_{\text{obs}} \circ$

838 \mathcal{S} regardless of which propagation effects (e.g. full waveform or Eikonal's equation
 839 for ray tracing, 1D or 3D) are considered. In seismology in general, we use some
 840 variations of quasi-Newton methods to linearize the inverse problem [Fuji *et al.*,
 841 2010; Konishi *et al.*, 2014; French and Romanowicz, 2015; Marjanović *et al.*, 2017;
 842 Xiao *et al.*, 2020].

- 843 (iv) Based on an understanding of petrology we can interpret the ensemble of seismic
 844 parameters as geodynamically meaningful parameters such as temperature and
 845 chemical anomaly inside the mantle. Look-up tables of C_S^D or C_D^S are produced
 846 based on either *in situ* experiments or numerical simulation in petrology such as
 847 first-principles *ab initio* calculations [Deschamps *et al.*, 2019; Konishi *et al.*, 2020].
- 848 (v) The geodynamicists can finally then seek the most probable scenario(s) of the Earth's
 849 inner evolution, mostly by trial-and-error forward modeling schemes and few by
 850 time-reversal or adjoint methods in geodynamics. Here, however, we denote this
 851 last step deliberately also as an inverse operator \mathcal{D}^\dagger since the aim is clearly to eval-
 852 uate the misfit of the geodynamical models to seismic tomographic "observation":

$$|\mathcal{D}(\mathbf{m}_{\text{inv}}) - C_S^D \circ \mathcal{S}^\dagger \circ \mathcal{F}_{\text{obs}}(\mathbf{d})|^\alpha \quad (\text{A.2})$$

853 with α a positive constant. We evaluate this misfit often in amplitude spectra or
 854 correlation domain [Steinberger and Torsvik, 2012]. Atkins *et al.* [2016] and Shah-
 855 nas *et al.* [2018] proposed a probabilistic inverse problem, by means of machine
 856 learning, to choose plausible scenarios \mathbf{m}_{inv} once we obtain tomographic "observa-
 857 tion" $C_S^D \circ \mathcal{S}^\dagger \circ \mathcal{F}_{\text{obs}}(\mathbf{d})$.

858 The workflow (eq. A.1) has been invaluable in geosciences since we have little data
 859 other than present-day seismological observation at seismic stations \mathbf{d} to infer the evolu-
 860 tion of the Earth's mantle \mathbf{m} . Statistical confidence of the seismic model $\mathcal{S}^\dagger \circ \mathcal{F}_{\text{obs}}(\mathbf{d})$ has
 861 increased not only due to the increasing number of seismic stations, including ocean bot-
 862 tom seismic arrays, but also due to the theoretical and numerical improvement of $\mathcal{F}_{\text{comp}} \circ \mathcal{S}$
 863 or a better estimation of $(\mathcal{F}_{\text{comp}} \circ \mathcal{S})^\dagger$.

864 The real data \mathbf{d} should be a function of the geodynamic parameters \mathbf{m}_{true} :

$$\mathbf{d} = \mathcal{S} \circ C_D^S \circ \mathcal{D}(\mathbf{m}_{\text{true}}), \quad (\text{A.3})$$

865 The “estimated” geodynamical parameters \mathbf{m}_{inv} are therefore “low resolution filtered” as
 866 follows:

$$\mathbf{m}_{\text{inv}} = \mathcal{D}^\dagger \circ C_S^D \circ \mathcal{S}^\dagger \circ \mathcal{F}_{\text{comp}}^\dagger \circ \mathcal{F}_{\text{obs}} \circ \mathcal{S} \circ C_D^S \circ \mathcal{D}(\mathbf{m}_{\text{true}}). \quad (\text{A.4})$$

867 When we consider only the seismic structure of the Earth’s interior, the resolution opera-
 868 tor,

$$\mathcal{R} = \mathcal{S}^\dagger \circ \mathcal{F}_{\text{comp}}^\dagger \circ \mathcal{F}_{\text{obs}} \circ \mathcal{S} \quad (\text{A.5})$$

869 is the same as the “seismic tomographic filter operator” proposed by [Ritsema *et al.*, 2007;
 870 Schuberth *et al.*, 2012; Koelemeijer *et al.*, 2018]. Evaluation of the “seismically filtered
 871 model”:

$$\mathbf{p} = \mathcal{R} \circ C_D^S \circ \mathcal{D}(\mathbf{m}) \quad (\text{A.6})$$

872 is interesting since it represents the sensitivity of our seismic tomographic model with
 873 respect to geodynamical model parameters.

874 Nevertheless, due to the non-linearity of each forward operator and the approxima-
 875 tions of its linearized inverse operator, it is difficult to quantitatively discuss the proba-
 876 bility of proposed Earth’s evolution scenarios. The only way to self-consistently answer
 877 this question is to directly model the full problem from first principles and compare the
 878 predicted data with the real data (eq. A.3), *i.e.* predict a self-consistent thermo-chemical
 879 structure, then predict the seismic properties and subsequently make a full comparison
 880 with the observation: the seismic signal received at the Earth’s surface. We must perform
 881 every procedure in a forward manner. This approach could be more powerful and objec-
 882 tive than a series of inversions (eq. A.1), in particular when we have concrete geodynami-
 883 cal parameters \mathbf{m} to look for.

884 Here in this paper, we propose to find the direct link between \mathbf{m} and \mathbf{d} by a series
 885 of forward modeling:

$$\mathbf{u} = \mathcal{S} \circ C_D^S \circ \mathcal{D}(\mathbf{m}) \quad (\text{A.7})$$

886 with \mathbf{u} the “seismically filtered waveform data” instead of “seismically filtered model”.
 887 Sensitivity analysis of \mathbf{u} as a function of \mathbf{m} is more straightforward than the evaluation of
 888 \mathbf{p} in eq. A.6. We then apply the \mathbf{u} with a new processing operator \mathcal{F} applied to synthetic
 889 and observed waveforms in order to compute the misfit function:

$$|\mathcal{F}(\mathbf{u}) - \mathcal{F}(\mathbf{d})|^\alpha = |\mathcal{F} \circ \mathcal{S} \circ C_D^S \circ \mathcal{D}(\mathbf{m}) - \mathcal{F}(\mathbf{d})|^\alpha. \quad (\text{A.8})$$

890 The workflow presented in A.8 is represented in Figure 1. As the direct comparison be-
891 tween \mathbf{d} and \mathbf{u} is hard to realize, as is also the case in eq. A.2, the choice of \mathcal{F} (the sim-
892 plification of the problem) is the key. In the methodology section, we will explain how to
893 connect realize the workflow (eq. A.8).

894 References

- 895 Armitage, J. J., D. J. Ferguson, S. Goes, J. Hammond, E. Calais, C. A. Rychert, and N. Harmon (2015),
 896 Upper mantle temperature and the onset of extension and break-up in afar, africa, *Earth Planet Sc
 897 Lett*, 418(Nature 465 2010), 78–90, doi:10.1016/j.epsl.2015.02.039.
- 898 Armitage, J. J., K. D. Petersen, and P. Marta (2018), The role of crustal strength in controlling magma-
 899 tism and melt chemistry during rifting and breakup, *Geochem Geophys Geosystems*, 19(2), 534–550,
 900 doi:10.1002/2017GC007326.
- 901 Asimow, P., M. Hirschmann, and E. Stolper (2001), Calculation of peridotite partial melting
 902 from thermodynamic models of minerals and melts, IV. adiabatic decompression and the
 903 composition and mean properties of mid-ocean ridge basalts, *J Petrol*, 42(5), 963–998, doi:
 904 10.1093/petrology/42.5.963.
- 905 Atkins, S., A. Valentine, P. Tackley, and J. Trampert (2016), Using pattern recognition to in-
 906 fer parameters governing mantle convection, *Phys. Earth Planet. Inter.*, 257, 171–186, doi:
 907 10.1016/j.pepi.2016.05.016.
- 908 Bormann, P., and E. Wielandt (2002), *Chapter 4 Seismic signals and noise*, pp. 1–62, 2 ed.
- 909 Buland, R., and C. Chapman (1983), The computation of seismic travel times, *Bull. Seismol. Soc. Am.*,
 910 73(5), 1271–1302.
- 911 Burley, J., and R. F. Katz (2015), Variations in mid-ocean ridge CO₂ emissions driven by glacial cy-
 912 cles, *Earth Planet Sc Lett*, 426(Nature 421 6925 2003), 246–258, doi:10.1016/j.epsl.2015.06.031.
- 913 Cammarano, F., S. Goes, P. Vacher, and D. Giardini (2003), Inferring upper-mantle temperatures from
 914 seismic velocities, *Phys Earth Planet In*, 138(3-4), 197–222, doi:10.1016/S0031-9201(03)00156-0.
- 915 Chantel, J., G. Manthilake, D. Andrault, D. Novella, T. Yu, and Y. Wang (2016), Experimental
 916 evidence supports mantle partial melting in the asthenosphere, *Sci Adv*, 2(5), e1600,246, doi:
 917 10.1126/sciadv.1600246.
- 918 Charvis, P., A. Laesapura, and J. Gallart (1999), Spatial distribution of hotspot material added to the
 919 lithosphere under la réunion, from wide-angle seismic data, *J. Geophys. Res. Solid Earth*, 104(B2),
 920 2875–2893, doi:10.1029/98JB02841.
- 921 Cobden, L., J. Trampert, and A. Fichtner (2018), Insights on upper mantle melting, rheology, and
 922 anelastic behavior from seismic shear wave tomography, *Geochemistry, Geophysics, Geosystems*,
 923 19(10), 3892–3916.
- 924 Connolly, J. (2005), Computation of phase equilibria by linear programming: A tool for geodynamic
 925 modeling and its application to subduction zone decarbonation, *Earth Planet Sc Lett*, 236(1-2), 524–

- 926 541, doi:10.1016/j.epsl.2005.04.033.
- 927 Connolly, J., M. Schmidt, G. Solferino, and N. Bagdassarov (2009), Permeability of astheno-
928 spheric mantle and melt extraction rates at mid-ocean ridges, *Nature*, 462(7270), 209–212, doi:
929 10.1038/nature08517.
- 930 Courtillot, V., A. Davaille, J. Besse, and J. Stock (2003), Three distinct types of hotspots in the earth's
931 mantle, *Earth Planet Sc Lett*, 205(3-4), 295–308, doi:10.1016/S0012-821X(02)01048-8.
- 932 Crotwell, H., T. Owens, and J. Ritsema (1999), The TauP toolkit: Flexible seismic travel-time and ray-
933 path utilities, *Seismol Res Lett*, 70(2), 154–160, doi:10.1785/gssrl.70.2.154.
- 934 Cummins, P., N. Takeuchi, and R. Geller (1997), Computation of complete synthetic seismograms for
935 laterally heterogeneous models using the direct solution method, *Geophys J Int*, 130(1), 1–16, doi:
936 10.1111/j.1365-246X.1997.tb00983.x.
- 937 Deschamps, F., K. Konishi, N. Fuji, and L. Cobden (2019), Radial thermo-chemical structure
938 beneath western and northern pacific from seismic waveform inversion, 520, 153–163, doi:
939 10.1016/j.epsl.2019.05.040.
- 940 Douet, V., M. Vallée, D. Zigone, S. Bonaimé, E. Stutzmann, A. Maggi, C. Pardo, A. Bernard, N. Leroy,
941 F. Pesqueira, et al. (2016), The geoscope broadband seismic observatory, in *EGU General Assembly
942 Conference Abstracts*, vol. 18.
- 943 Duncan, R., and R. Hargraves (1990), 40Ar/39Ar geochronology of basement rocks from the mas-
944 carene plateau, the chagos bank, and the maldives ridge, *Proc Ocean Drill Prog Sci Results*, 115,
945 43–51.
- 946 Eilon, Z. C., and G. A. Abers (2017), High seismic attenuation at a mid-ocean ridge reveals the distri-
947 bution of deep melt, *Sci Adv*, 3(5), e1602,829, doi:10.1126/sciadv.1602829.
- 948 Elliott, T., and M. Spiegelman (2003), Melt migration in oceanic crustal production: a u-series perspec-
949 tive, *Treatise on geochemistry*.
- 950 Fontaine, F. R., G. Barruol, H. Tkalčić, I. Wölbern, G. Rümpker, T. Bodin, and M. Haugmar (2015),
951 Crustal and uppermost mantle structure variation beneath la réunion hotspot track, *Geophys J Int*,
952 203(1), 107–126, doi:10.1093/gji/ggv279.
- 953 Forsyth, D. (1998), Imaging the deep seismic structure beneath a Mid-Ocean ridge: The MELT experi-
954 ment, *Science*, 280(5367), 1215–1218, doi:10.1126/science.280.5367.1215.
- 955 French, S., and B. Romanowicz (2015), Broad plumes rooted at the base of the earth's mantle beneath
956 major hotspots, *Nature*, 525, 95–99.
- 957 Fuji, N., K. Kawai, and R. Geller (2010), A methodology for inversion of broadband seismic wave-
958 forms for elastic and anelastic structure and its application to the mantle transition zone beneath the

- 959 northwestern pacific, *Phys. Earth Planet. Inter.*, 180, 118–137.
- 960 Fuji, N., S. Chevrot, L. Zhao, R. J. Geller, and K. Kawai (2012), Finite-frequency structural sensitivi-
961 ties of short-period compressional body waves, *Geophys J Int*, 190(1), 522–540, doi:10.1111/j.1365-
962 246X.2012.05495.x.
- 963 Gallart, J., L. Driad, P. Charvis, and M. Sapin (1999), Perturbation to the lithosphere along the hotspot
964 track of la réunion from an offshore-onshore seismic transect, *J. Geophys. Res.*, 104(B2), 2895–
965 2908, doi:10.1029/98JB02840.
- 966 Geller, R., and T. Ohminato (1994), Computation of synthetic seismograms and their partial derivatives
967 for heterogeneous media with arbitrary natural boundary conditions using the direct solution . . . ,
968 *Geophys. J. Int.*, 116, 421–446.
- 969 Geller, R., and N. Takeuchi (1995), A new method for computing highly accurate DSM synthetic seis-
970 mograms, *Geophysical Journal International*, doi:10.1111/j.1365-246X.1995.tb06865.x.
- 971 Geller, R., and N. Takeuchi (1998), Optimally accurate second-order time-domain finite difference
972 scheme for the elastic equation of motion: one-dimensional cases, *Geophysical Journal Interna-*
973 *tional*.
- 974 Ghiorso, M. S., and R. O. Sack (1995), Chemical mass transfer in magmatic processes IV. a revised and
975 internally consistent thermodynamic model for the interpolation and extrapolation of liquid-solid
976 equilibria in magmatic systems at elevated temperatures and pressures, *Contrib Mineral Petr*, 119(2-
977 3), 197–212, doi:10.1007/BF00307281.
- 978 Goes, S., J. Armitage, N. Harmon, H. Smith, and R. Huismans (2012), Low seismic velocities be-
979 low mid-ocean ridges: Attenuation versus melt retention, *J Geophys Res Solid Earth* 1978 2012,
980 117(B12), n/a–n/a, doi:10.1029/2012JB009637.
- 981 Hammond, W., and E. Humphreys (2000), Upper mantle seismic wave velocity: Effects of realistic
982 partial melt geometries, *J. Geophys. Res.*, 105(B5), 10,975–10,986, doi:10.1029/2000JB900041.
- 983 Harmon, N., D. W. Forsyth, and D. S. Weeraratne (2009), Thickening of young pacific lithosphere from
984 high-resolution rayleigh wave tomography: A test of the conductive cooling model, *Earth Planet Sc*
985 *Lett*, 278(1-2), 96–106, doi:10.1016/j.epsl.2008.11.025.
- 986 Hasegawa, K., N. Fuji, and K. Konishi (2018), Improvement of accuracy of the spectral element
987 method for elastic wave computation using modified numerical integration operators, *Comp. Meth-*
988 *ods Appl. Mech. Eng.*, 342, 200–223.
- 989 Havlin, C., and E. Parmentier (2014), Implications for melt transport and source heterogeneity in up-
990 welling mantle from the magnitude of sp converted phases generated at the onset of melting, *Geo-*
991 *phys Res Lett*, 41(15), 5444–5450, doi:10.1002/2014GL060890.

- 992 Herzberg, C., P. Asimow, N. Arndt, Y. Niu, C. Lesher, J. Fitton, M. Cheadle, and A. Saunders (2007),
993 Temperatures in ambient mantle and plumes: Constraints from basalts, picrites, and komatiites,
994 *Geochem Geophys Geosystems*, 8(2), n/a–n/a, doi:10.1029/2006GC001390.
- 995 Herzberg, C., P. D. Asimow, D. A. Ionov, C. Vidito, M. G. Jackson, and D. Geist (2013), Nickel and
996 helium evidence for melt above the core–mantle boundary, *Nature*, 493(7432), 393–397.
- 997 Hewitt, I. J. (2010), Modelling melting rates in upwelling mantle, *Earth Planet Sc Lett*, 300(3-4), 264–
998 274, doi:10.1016/j.epsl.2010.10.010.
- 999 Hirose, K., and I. Kushiro (1993), Partial melting of dry peridotites at high pressures: Determination of
1000 compositions of melts segregated from peridotite using aggregates of diamond, *Earth Planet Sc Lett*,
1001 114(4), 477–489, doi:10.1016/0012-821X(93)90077-M.
- 1002 Hirschmann, M., M. Ghiorso, and M. Stolper (1999), Calculation of peridotite partial melting from
1003 thermodynamic models of minerals and melts. II. isobaric variations in melts near the solidus and
1004 owing to variable source composition, *J Petrol*, 40(2), 297–313, doi:10.1093/petroj/40.2.297.
- 1005 Hirschmann, M., T. Tenner, C. Aubaud, and A. Withers (2009), Dehydration melting of nominally
1006 anhydrous mantle: The primacy of partitioning, *Phys Earth Planet In*, 176(1-2), 54–68, doi:
1007 10.1016/j.pepi.2009.04.001.
- 1008 Karato, S. (1993), Importance of anelasticity in the interpretation of seismic tomography, *Geophysical*
1009 *Research Letters*, doi:10.1029/93GL01767@10.1002/(ISSN)1944-8007.GRL40.
- 1010 Karato, S.-i. (2014), Does partial melting explain geophysical anomalies?, *Phys Earth Planet In*, 228,
1011 300–306, doi:10.1016/j.pepi.2013.08.006.
- 1012 Katz, R. F., M. Spiegelman, and C. H. Langmuir (2003), A new parameterization of hydrous mantle
1013 melting, *Geochem Geophys Geosystems*, 4(9), n/a–n/a, doi:10.1029/2002GC000433.
- 1014 Kawai, K., N. Takeuchi, and R. J. Geller (2006), Complete synthetic seismograms up to 2 hz for trans-
1015 versely isotropic spherically symmetric media, *Geophys J Int*, 164(2), 411–424, doi:10.1111/j.1365-
1016 246X.2005.02829.x.
- 1017 Kennett, B., E. Engdahl, and R. Buland (1995), Constraints on seismic velocities in the earth from trav-
1018 eltimes, *Geophys J Int*, 122(1), 108–124, doi:10.1111/j.1365-246X.1995.tb03540.x.
- 1019 Koelemeijer, P., B. Schuberth, D. Davies, A. Deuss, and J. Ritsema (2018), Constraints on the presence
1020 of post-perovskite in earth’s lowermost mantle from tomographic-geodynamic model comparisons,
1021 *Earth Planet. Sci. Lett.*, 494, 226–238.
- 1022 Komatitsch, D., and J. Vilotte (1998), The spectral element method: an efficient tool to simulate the
1023 seismic response of 2d and 3d geological structures, *Bull. Seis. Soc. Am.*, 88, 368–392.

- 1024 Konishi, K., K. Kawai, R. Geller, and N. Fuji (2014), Waveform inversion for localized three-
1025 dimensional seismic velocity structure in the lowermost mantle beneath the western pacific, *Geo-*
1026 *phys. J. Int.*, 199, 1245–1267.
- 1027 Konishi, K., N. Fuji, and F. Deschamps (2020), Three-dimensional elastic and anelastic structure
1028 of the lowermost mantle beneath the western pacific from finite-frequency tomography, doi:
1029 10.1029/2019JB018089.
- 1030 Marjanović, M., N. Fuji, S. Singh, T. Belahi, and J. Escartín (2017), Seismic signatures of hydrother-
1031 mal pathways along the east pacific rise between 9° 16' e and 9° 56' n, *J. Geophys. Res.*, 122,
1032 10,241–10,262.
- 1033 Mazzullo, A., E. Stutzmann, J. Montagner, S. Kiselev, S. Maurya, G. Barruol, and K. Sigloch (2017),
1034 Anisotropic tomography around la réunion island from rayleigh waves, *J Geophys Res Solid Earth*,
1035 122(11), 9132–9148, doi:10.1002/2017JB014354.
- 1036 McKenzie, D. (1984), The generation and compaction of partially molten rock, *J Petrol*, 25(3), 713–
1037 765, doi:10.1093/petrology/25.3.713.
- 1038 Mehouachi, F., and S. C. Singh (2018), Water-rich sublithospheric melt channel in the equatorial at-
1039 lantic ocean, *Nat Geosci*, 11(1), 65–69, doi:10.1038/s41561-017-0034-z.
- 1040 Miller, K. J., W.-I. Zhu, L. Montési, and G. A. Gaetani (2014), Experimental quantification of
1041 permeability of partially molten mantle rock, 388(*J. Geophys. Res.* 100 1995), 273–282, doi:
1042 10.1016/j.epsl.2013.12.003.
- 1043 Monteiller, V., S. Chevrot, D. Komatitsch, and Y. Wang (2015), Three-dimensional full waveform in-
1044 version of short-period teleseismic wavefields based upon the sem-dsm hybrid method, *Geophysical*
1045 *Journal International*, 202(2), 811–827.
- 1046 Morgan, J. (2001), Thermodynamics of pressure release melting of a veined plum pudding mantle,
1047 *Geochem Geophys Geosystems*, 2(4), n/a–n/a, doi:10.1029/2000GC000049.
- 1048 Ribe, N. (1985), The deformation and compaction of partial molten zones, *Geophysical Journal Inter-*
1049 *national*, doi:10.1111/j.1365-246X.1985.tb06499.x.
- 1050 Richards, M., R. Duncan, and V. Science (1989), Flood basalts and hot-spot tracks: plume heads and
1051 tails, *Science*, doi:10.1126/science.246.4926.103.
- 1052 Richards, M., C. Eduardo, L. Carolina, M. Ghiorso, and L. Stixrude (2013), Petrological interpretation
1053 of deep crustal intrusive bodies beneath oceanic hotspot provinces, *Geochem Geophys Geosystems*,
1054 14(3), 604–619, doi:10.1029/2012GC004448.
- 1055 Ritsema, J., A. McNamara, and A. Bull (2007), Tomographic filtering of geodynamic models: impli-
1056 cations for model interpretation and large-scale mantle structure, *J. Geophys. Res.*, 112, B01,303,

- 1057 doi:10.1029/2006JB004566.
- 1058 Rychert, C. A., J. O. Hammond, N. Harmon, M. J. Kendall, D. Keir, C. Ebinger, I. D. Bastow, A. Ayele,
1059 M. Belachew, and G. Stuart (2012), Volcanism in the afar rift sustained by decompression melting
1060 with minimal plume influence, *Nat Geosci*, 5(6), 406–409, doi:10.1038/ngeo1455.
- 1061 Rychert, C. A., G. Laske, N. Harmon, and P. M. Shearer (2013), Seismic imaging of melt in a displaced
1062 hawaiian plume, *Nat Geosci*, 6(8), 657–660, doi:10.1038/ngeo1878.
- 1063 Rychert, C. A., N. Harmon, and C. Ebinger (2014), Receiver function imaging of lithospheric structure
1064 and the onset of melting beneath the galápagos archipelago, *Earth Planet Sc Lett*, 388, 156–165,
1065 doi:10.1016/j.epsl.2013.11.027.
- 1066 Schuberth, B. S., C. Zaroli, and G. Nolet (2012), Synthetic seismograms for a synthetic earth: long-
1067 period p- and s-wave traveltimes can be explained by temperature alone, *Geophys J Int*,
1068 188(3), 1393–1412, doi:10.1111/j.1365-246X.2011.05333.x.
- 1069 Scott, D. (1992), Small-scale convection and mantle melting beneath mid-ocean ridges, *Washington
1070 DC American Geophysical Union*
- 1071 Shahnas, M., D. Yuen, and R. Pysklywec (2018), Inverse problems in geodynamics using machine
1072 learning algorithms, *J. Geophys. Res. Solid Earth*, 123, 296–310, doi:10.1002/2017JB014846.
- 1073 Sobolev, A., and I. Nikogosian (1994), Petrology of long-lived mantle plume magmatism: Hawaii,
1074 pacific and reunion island, indian ocean, *Petrology*.
- 1075 Steinberger, B., and T. Torsvik (2012), A geodynamic model of plumes from the margins of large low
1076 shear velocity provinces, *Geoch. Geophys. Geosys.*, 13, Q01W09, doi:10.1029/2011GC003808.
- 1077 Stixrude, L., and C. Lithgow-Bertelloni (2005), Thermodynamics of mantle minerals – i. physical prop-
1078 erties, *Geophys J Int*, 162(2), 610–632, doi:10.1111/j.1365-246X.2005.02642.x.
- 1079 Stracke, A., B. Bourdon, and M. Dan (2006), Melt extraction in the earth's mantle: Constraints
1080 from U–Th–Pa–Ra studies in oceanic basalts, *Earth Planet Sc Lett*, 244(1-2), 97–112, doi:
1081 10.1016/j.epsl.2006.01.057.
- 1082 Vallée, M., and V. Douet (2016), A new database of source time functions (STFs) extracted from the
1083 SCARDEC method, *Phys Earth Planet In*, 257, 149–157, doi:10.1016/j.pepi.2016.05.012.
- 1084 Weatherley, S. M., and R. F. Katz (2016), Melt transport rates in heterogeneous mantle beneath mid-
1085 ocean ridges, *Geochim Cosmochim Ac*, 172, 39–54, doi:10.1016/j.gca.2015.09.029.
- 1086 Xiao, Z., N. Fuji, T. Iidaka, Y. Gao, X. Sun, and Q. Liu (2020), Seismic structure beneath the tibetan
1087 plateau from iterative finite-frequency tomography based on chinarray: New insights into the indo-
1088 asian collision, doi:10.1029/2019JB018344.

- 1089 Xu, W., C. Lithgow-Bertelloni, L. Sixtrude, and J. Ritsema (2008), The effect of bulk composition
1090 and temperature on mantle seismic structure, *Earth and Planetary Science Letters*, 275, 70–79, doi:
1091 10.1016/j.epsl.2008.08.012.
- 1092 Zhu, W., and G. Hirth (2003), A network model for permeability in partially molten rocks, *Earth*
1093 *Planet Sc Lett*, 212(3-4), 407–416, doi:10.1016/S0012-821X(03)00264-4.